Structural basis of p62/SQSTM1 helical filaments, their presence in p62 bodies and role in cargo recognition in the cell

Arjen J. Jakobi[1,2,3‡], Stefan T. Huber[1†‡], Simon A. Mortensen[1,4,5†], Sebastian W. Schultz[6], Anthimi Palara[7], Tanja Kuhm[1‡], Birendra Kumar Shrestha[7], Trond Lamark[7], Wim J.H. Hagen[1], Matthias Wilmanns[2,3], Terje Johansen[7], Andreas Brech[6], Carsten Sachse[1,4,5*]

[1] European Molecular Biology Laboratory (EMBL), Structural and Computational Biology Unit, Meyerhofstraße 1, 69117 Heidelberg, Germany

[2] European Molecular Biology Laboratory (EMBL), Hamburg Unit c/o DESY, Notkestraße 85, 22607 Hamburg, Germany

[3] The Hamburg Centre for Ultrafast Imaging (CUI), Luruper Chaussee 149, 22761 Hamburg, Germany

[4] Ernst-Ruska Centre for Microscopy and Spectroscopy with Electrons (ER-C-3/Structural Biology), Forschungszentrum Jülich, 52425 Jülich, Germany

[5] JuStruct: Jülich Center for Structural Biology, Forschungszentrum Jülich, 52425 Jülich, Germany.

[6] Department of Molecular Cell Biology, Institute for Cancer Research, Oslo University Hospital, Montebello, N-0379 Oslo, Norway.

[7] Molecular Cancer Research Group, Institute of Medical Biology, University of Tromsø – The Arctic University of Norway, 9037 Tromsø, Norway

[‡] Current address: Department of Bionanoscience, Kavli Institute of Nanoscience, Delft University of Technology, Van der Maasweg 9, 2629 HZ Delft, Netherlands

[†] These authors contributed equally

* Correspondence should be addressed to: c.sachse@fz-juelich.de

Keywords

PB1 domain, p62/SQSTM1, helical filaments, p62 bodies, phase separation, cargo recognition, autophagy

Abstract

p62/SQSTM1 is an autophagy receptor and signaling adaptor with an N-terminal PB1 domain that forms the scaffold of phase-separated p62 bodies in the cell. The molecular determinants that govern PB1 domain filament formation *in vitro* remain to be determined and the role of p62 filaments inside the cell is currently unclear. We determined four high-resolution cryo-EM structures of different human and Arabidopsis PB1 domain assemblies and observed a filamentous ultrastructure of phase-separated p62/SQSTM1 bodies using correlative cellular EM. We show that oligomerization or polymerization, driven by a double arginine finger in the PB1 domain, is a general requirement for lysosomal targeting of p62. Furthermore, the filamentous assembly state of p62 is required for autophagosomal processing of the p62-specific cargo KEAP1. Our results show that using such mechanisms, p62 filaments can be critical for cargo recognition and are an integral part of phase separated p62 bodies.

Introduction

p62/SQSTM1 (from here on p62) is a multifunctional adaptor protein that acts as a central scaffold protein in different cellular processes such as autophagy and signaling (Katsuragi, et al. 2015). p62 has a tendency to cluster and in human cells is often observed in discrete punctae known as p62 bodies (Lamark et al., 2003). The formation of these bodies is dependent on the amino-terminal PB1 domain of p62 (Cheng, 2015; Lamark et al., 2003). PB1 domains are protein interaction modules with critical roles in the assembly of protein complexes involved in autophagy, signaling, cell division and redox processes (Moscat et al., 2006), as well as the auxin response pathway in plants (Korasick et al. 2014). PB1 domains form homotypic interactions via conserved electrostatic motifs molded by basic or acidic surface patches on opposite faces of their ubiquitin-like β-grasp fold (Lamark et al., 2003; Wilson et al., 2003). According to their interaction profile, PB1 domains are classified into type A (acidic, OPCA motif), type B (basic) or mixed type AB members (Wilson et al., 2003). While type A and type B PB1 domains can form heterodimeric protein complexes, type AB members can mediate interactions with either PB1 domain type or engage in homotypic interactions to form homo-oligomers or hetero-oligomers (Lamark et al., 2003; Sumimoto et al., 2007). More recently, PB1-mediated self-interaction of p62/SQSTM1 was found to result in the formation of filamentous polymers (Paine et al., 2005) with helical symmetry *in vitro* (Ciuffa et al., 2015).

p62 has been shown to function in autophagy and cellular signalling. Autophagy is a degradative cellular housekeeping pathway by which cytoplasmic materials are engulfed in a double membrane vesicle termed the autophagosome and delivered to the lysosomal compartment (Mizushima and Komatsu, 2011). Substrates for autophagy are not limited by molecular size and include large protein aggregates, intracellular pathogens and cellular organelles. Selective autophagy has been characterized as the process that specifically directs cytosolic substrates to the formation site of autophagosomal membranes (Johansen and Lamark, 2011; Kraft et al., 2010). As an autophagy receptor,

p62 links cargo proteins with the autophagosome membrane (Pankiv et al., 2007). PB1-mediated oligomerization of p62 is essential for its function as a selective autophagy receptor (Itakura and Mizushima, 2011) and thought to facilitate co-aggregation of ubiquitylated cargo (Wurzer et al., 2015). The C-terminal UBA domain of p62 captures ubiquitinated cargo and the LIR motif guides the cargo-receptor complex to Atg8/LC3, which is anchored to the surface of the autophagosomal membrane (Bjørkøy et al., 2005; Pankiv et al., 2007). In signalling, p62 bodies constitute an interaction hub for the kinases MEKK3, MEK5 and aPKCs, which also contain PB1 domains (Lamark et al., 2003), in addition to triggering the NFκB pathway through the polyubiquitination of tumor necrosis factor (TNF) receptor-associated factor 6 (TRAF6) (Duran et al., 2008).

Due to p62's involvement in protein homeostasis, the impairment of autophagy or oxidative stress results in aggregation or upregulation of p62 including increased body formation (Carroll et al., 2018; Sukseree et al., 2018). Recently, we and others independently found that p62 reconstituted with other components of the autophagy pathway, such as ubiquitinated model cargo and the selective autophagy receptor NBR1, spontaneously coalesces into p62 bodies *in vitro* (Zaffagnini et al., 2018) and shows the characteristics of liquid-liquid phase separation *in vivo* (Sun et al., 2018). These studies established that oligomerization by the N-terminal PB1 domain of p62 is an essential requirement for recapitulating phase separation *in vitro* as well as for cargo uptake *in vivo* (Sun et al., 2018, Britzen-Laurent et al., 2010; Itakura and Mizushima, 2011).

The exact structural requirements and physiological conditions under which p62-PB1 domains self-assemble or engage in hetero-PB1 complexes are currently unclear. Furthermore, it is not known what assembly state of p62 is required for biological functions such as cargo uptake in autophagy or the formation of phase-separated compartments *in vivo*. Based on high-resolution electron cryo-microscopy (cryo-EM) and crystal structures, cellular EM,

biochemical and cellular characterization, we here reveal the structural basis for polymeric PB1 self-assembly and define the relevance of symmetry and spatial arrangement of the polymeric assembly state for p62 autophagy function *in vivo*.

Results

p62, TFG-1 and AtNBR1 PB1 domains form filamentous homo-polymers

Based on our previous finding that p62 is capable of forming homo-oligomeric filamentous assemblies (Ciuffa et al., 2015), we set out to understand whether related AB-type PB1 domains possess a similar property to self-assemble. With reference to sequence alignments, we expressed and purified PB1 domains from human p62$^{1-102}$, p62$^{1-122}$, TFG-1$^{1-95}$ (Trk-fused gene 1), the atypical protein kinases PKCζ$^{11-101}$ as well as the evolutionary related PB1 domain of the NBR1$^{1-95}$ autophagy receptor from *Arabidopsis thaliana* (AtNBR1) (Svenning et al., 2011) (**Figure 1A**). p62, TFG-1, PKCζ and AtNBR1 are multi-domain proteins that share the N-terminal PB1 domain with additional functional C-terminal domains (**Figure 1B**). In order to assess whether these PB1 domain containing proteins are capable of forming high-molecular weight assemblies, we performed sedimentation assays by ultracentrifugation. The PB1 domains of TFG-1$^{1-95}$, AtNBR1$^{1-95}$, p62$^{1-102}$ and p62$^{1-122}$ were found in the pellet fraction, whereas PB1 domains from PKCζ remained soluble (**Figure 1C**). We visualized the pelleted fractions using negative staining electron microscopy (EM) and observed elongated filamentous or tubular assemblies for the PB1 domains of p62$^{1-122}$, TFG-1 and AtNBR1 that measure 145 ± 5, 900 ± 52 and 120 ± 4 Å in diameter, respectively (**Figure 1D**). Closer inspection of the sequence alignments revealed that all three of these PB1 domains share the tandem arginine motif close to the canonical lysine residue of the basic motif in B-type PB1 domains. By contrast, this tandem arginine motif is absent in AB-type PB1 sequences of PKCζ that does not form filamentous or tubular structures, suggesting a critical role for self-assembly.

Cryo-EM structures of AtNBR1 and p62-PB1 filaments

Of the three PB1 assemblies studied, AtNBR1$^{1-95}$ (AtNBR1-PB1) and p62$^{1-122}$ (p62-PB1) formed homogeneous filaments of constant diameter that appeared best suited for high-resolution structure investigation by cryo-EM. Therefore, we vitrified filaments of purified AtNBR1-PB1 and p62-PB1 domains and imaged the samples by cryo-EM (**Figure 2A/B**). Image classification of segmented PB1 helices revealed that both AtNBR1-PB1 and p62-PB1polymerize in two different tubular morphologies: a projection class with a ladder-like pattern we term L-type and a projection class with a serpent-like one we term S-type (**Figure 2C and Figure S1A-C**). L-type and S-type helices partition approximately evenly, i.e. 40% to 60% and 55% to 45% for p62-PB1 and AtNBR1-PB1 samples respectively. Further analysis revealed that the occurrence of L-type or S-type assemblies is persistent along the individual helices in micrographs of AtNBR1-PB1 whereas for p62-PB1 filaments regularly displayed transitions from L-type to S-type symmetry (**Figure S1D**). In an effort to understand the underlying structures of L-type and S-type projections, we analyzed the averaged power spectra from in-plane rotated segments and from class averages. The best Fourier spectra of AtNBR1-PB1 and p62-PB1 showed discrete layer-line reflections up to 5.9 and 4.7 Å suggesting a helical organization and preservation of structural order up to high resolution (**Figure S1E-F**). The comparison of the Fourier spectra confirmed that L-type and S-type structures are differently organized in their helical lattice. By indexing the layer lines in the Fourier spectra of AtNBR1-PB1 filaments, we concluded that L-type is a 2-stranded helix with a pitch of 77.2 Å and 11.47 subunits/turn, whereas S-type is a single double-strand helix with a pitch of 68.2 Å and 11.55 subunits/turn. For p62-PB1, we observed a 4-stranded L-type assembly and a 3-stranded S-type assembly. In the latter S-type, one of the three helical rungs is propagating in an antiparallel orientation, related to the central rung by local dihedral symmetry. The L-type here has a pitch of 135.9 Å with 14.16 subunits/turn and S-type has a pitch of 138.6 Å with 14.16 subunits/turn. Using the derived symmetries, we determined the 3.5/3.9 (L-type, p62/AtNBR1) and 4.0/4.4 Å (S-type, p62/AtNBR1) resolution structures

(**Figure 2C and Figure S1G-H**). All four structures form tubules of approximately 120 Å and 150 Å width with an inner diameter of 45 Å and 70 Å for AtNBR1-PB1 and p62-PB1, respectively. In all reconstructions, the main chain of the PB1 domain could be resolved with α-helical pitch features and individual β-strands separated. The overall fold of the asymmetric unit was found compatible with the NMR structure of the p62 PB1 monomer (Saio et al., 2009; 2010) (**Figure 3A/B**). In the absence of prior structural information, we traced the AtNBR1-PB1 *de novo*. This *de novo*-built model is in close agreement with the 1.6 Å crystal structure of a polymerization-deficient AtNBR1-PB1 mutant, which we solved in parallel (**Figure S2A, Table 1**). The relative orientation between adjacent subunits is very similar in the respective S-type and L-type assemblies of AtNBR1-PB1 and p62-PB1 (**Figure S2B)**. The β1-α1 loop in p62 is flexible and only visible in the L-type assembly density (**Figure S2C**). Expanding the asymmetric unit using the helical parameters of the L-type and S-type structures allowed analysis of the interface between repeating units. Despite overall similar interaction modes, the AtNBR1 and p62 assemblies showed differences in relative domain rotation between adjacent subunits and with respect to the helical axis (**Figure 3C**). In agreement with sequence analysis (see **Figure 1A**), the electrostatic potential mapped onto the molecular surface of the structures revealed that opposing charged surfaces mediate the PB1-PB1 interactions in the helical repeat (**Figure 3D**). In addition, we more closely examined the interface of homomeric interactions in the helical assemblies. The main interactions are formed between a double arginine finger formed by two neighboring arginine residues in strand β2 (R19-R20^{AtNBR1}/R20-21^{p62}) stabilizing strong salt-bridges to acidic residues (D60/D62/D64/D73^{AtNBR1} or D69/D71/D73/E82^{p62}) in the OPCA motif located in the β2-β3 loop and the α2 helix (**Figure 3E**). These interactions are assisted by the canonical type B lysine (K11^{AtNBR1} and K7^{p62}) in strand β1. Free energy calculations using the PDBePISA server (Krissinel and Henrick, 2007) suggest that a large part of the interface free energy is contributed by the double arginine finger. In addition to the canonical transverse interactions, the helices are further stabilized by longitudinal interactions Y14^{AtNBR1}/N28^{AtNBR1} or K102^{p62}/D92^{p62} and

R59^{p62}/D93^{p62} to subunits of neighboring strands along the helical axis (**Figure S2D/E**). The importance of electrostatic interactions on filament stability is further supported by the observation that increased ionic strength impedes stable filament formation and is sensitive to pH (**Figure S3A-H**). To validate our structural interpretation, we performed pull-down experiments using MBP-tagged wild-type AtNBR1-PB1 as a prey and a series of AtNBR1-PB1 interface mutants as bait (**Figure 3F**). All interface mutants decrease binding significantly compared with the wild-type and binding is completely abrogated in mutants lacking the double arginine finger, in agreement with observations in cellular assays (Svenning et al. 2011; Lamark et al., 2003). Together, the cryo-EM structures of two PB1 domain assemblies reveal that in addition to the canonical type electrostatic AB interactions the self-polymerization property is linked to the presence of a double arginine finger.

p62-PB1 domain interactions in the context of filamentous assemblies

After establishing the molecular basis of PB1 domain homo-polymerization, we wanted to understand how these assemblies interact with other PB1 domains of the A and B type that have been shown to co-localize with p62 punctae (Lamark et al., 2003). We therefore expressed and purified A-type human PB1 domains of MEK5$^{5-108}$ and NBR1$^{1-85}$, the B-type PB1 domain of MEKK3$^{43-127}$ and the AB-type PB1 domain of PKCζ$^{11-101}$ and determined their binding affinities for polymerization-deficient p62$^{1-102}$ (D69A/D73A) (Wilson et al., 2003) by isothermal titration calorimetry (ITC). These PB1 domains show 2-10 fold lower binding affinity to p62 compared with its self-interaction dissociation constant (K_D) of 6 nM (Ren et al., 2014), with K_D of 8.9 ± 0.9 nM, 12.6 ± 0.4 nM, 26.8 ± 0.5 nM, and 105 ± 1.3 nM determined for PKCζ (Ren et al., 2014), NBR1, MEKK3, and MEK5, respectively (**Figure 4A**). We therefore hypothesized that binding of these PB1 domain could compete with p62 self-polymerization and affect the assembly structures of p62-PB1 filaments. We found that NBR1-PB1 strongly interacts with p62-PB1 filaments and shortens p62-PB1 filaments on average to less than half the starting length (**Figure 4B/C**). Surprisingly, MEKK3, MEK5 and PKCζ-PB1 showed no effect on the pelletation behavior of p62 assemblies although having only marginally lower affinities than NBR1

(**Figure 4D**). To further analyze the interactions, we turned to negative staining EM. In agreement with the co-sedimentation data, for PB1 domains other than NBR1 we did not observe any effect on the morphology of p62 PB1 filaments and the measured filament lengths. In order to increase the sensitivity of detecting interactions with p62-PB1 filaments, we also imaged p62-PB1 filaments incubated with nanogold-labeled NBR1, MEKK3, MEK5 and PKCζ PB1 domains using negative staining EM (**Figure 4E**). For all PB1 domains, the micrographs confirmed end-on binding of the PB1 domains to p62-PB1 polymers or to oligomeric, ring-like structures. Interestingly, NBR1, MEK5, PKCζ PB1 domains preferably bind to one end of the filament (**Figure 4F**) consistent with an overall polar assembly observed in the 3D reconstructions of p62-PB1 filaments (see **Figure 2**). MEKK3-PB1 (type B) was not observed at p62-PB1 filament ends, but occasionally found at oligomeric ring-like structures. Biochemical interaction studies suggest that assembled filamentous p62 can display significantly lower apparent binding affinities for interacting PB1 domains than when present in the monomeric form.

Cellular p62 bodies consist of filamentous structures

Although self-oligomerization of p62 has been shown to be essential for targeting of p62 to the autophagosome (Itakura and Mizushima, 2011), it is unclear whether the filamentous assemblies observed *in vitro* are involved in this process or even occur inside of cells. We used correlative light and electron microscopy (CLEM) to study the ultrastructure of p62 bodies in a targeted manner. In order to enrich endogenous p62 bodies in RPE1 cells, we overexpressed a human NBR1 D50R mutant that abolishes the interaction with p62 (Lamark et al., 2003). Co-sedimentation experiments in which the relative amount of p62 in the monomeric and polymeric state are determined indeed showed that wild-type NBR1 solubilizes filamentous p62-PB1 whereas the D50R mutant does not (**Figure 5A**). In RPE1 cells, the NBR1-D50R mutant consistently produced larger p62 clusters possibly by promoting self-polymerization as observed *in vitro* (**Figure S4A**). In such cells, we localized p62 to punctate areas of 0.5 ± 0.1 µm diameter by fluorescence microscopy and visualized their ultrastructure by electron tomography (**Figure 5B** and

Figure S4B/C). The electron micrographs revealed that p62 bodies have a distinct appearance that is well differentiable from the cytosol with an electron-dense boundary of approx. 60 nm thickness surrounding the body (**Figure 5C/D**). We thresholded the interior density and found the p62 bodies are composed of a dense meshwork of filamentous assemblies (**Figure 5E**). Quantitative analysis of thresholded images confirmed the presence of elongated filament-like structures with an average diameter of 15 nm compatible in dimensions with the helical p62 structures observed *in vitro* (Ciuffa et al, 2015). We estimated the length of these structures by tracing individual filaments in sequential tomogram slices (**Figure 5F**). CLEM visualization of p62 bodies in cells under endogenous p62 levels confirm the presence of filamentous assemblies.

The effect of different p62's assemblies on autophagy clearance and lysosomal targeting of KEAP1

We next set out to assess the relevance of symmetry and assembly state of PB1-mediated filament assemblies for biological function within cellular p62 bodies and lysosomal targeting through the autophagy pathway. In the comparison of PB1 assemblies visualized by negative staining EM, TFG1 showed the most striking difference to p62 assemblies both in size and apparent symmetry (see **Figure 1D**). Therefore, we generated two p62 chimeras by fusing the TFG-PB1 domain to either p62(123-408) or p62Δ123-319 (mini-p62), containing only the p62 LIR motif and UBA domain) (**Figure 6A**) and visualized the resulting assemblies by negative staining EM (**Figure 6B)**. The TFG-1:p62 chimera forms 48 nm wide filaments, which is approximately three times the diameter of WT-p62 filaments and possesses a helical architecture clearly different from that of WT-p62 filaments. The TFG1-mini-p62 chimera forms defined, ring-shaped oligomers with ~12 nm in diameter. To test whether the TFG1-p62 fusion constructs are able to form p62 bodies in cells, we expressed the chimeras fused to an N-terminal GFP tag in HeLa cells deficient of endogenous p62. As controls we also expressed GFP-tagged WT p62 and the mini-p62 construct (p62Δ123-319) (**Figure 6C**). The transfected cells were analyzed by confocal fluorescence microscopy 24 h and

48 h post transfection. All constructs formed p62 bodies with the majority of dots having a diameter in the range 0.1 to 0.5 µm. We further classified GFP-positive punctae according to frequency of occurrence, the tendency to cluster and the morphological appearance (**Figure 6C-D and Figure S5F**).

We next asked whether TFG1-p62 could perform the biological function of p62. We first assessed whether TFG1-p62 can be turned over by autophagy and targeted to acidified cellular compartments by using the “traffic light” reporter. Here, the mCherry-YFP tandem tag is fused to the target protein and the acidification of the construct in lysosomes is monitored by appearance of red punctae. Although both TFG1-p62 chimera displayed a diffuse yellow fraction, they were almost as efficiently degraded by autophagy as the WT and mini-p62 constructs (**Figure 6E-F, Figure S5A-D**). We then asked if the TFG-p62 chimera were able to act as cargo receptor for a p62-specific substrate, KEAP1, and mediate autophagy degradation (Jain et al., 2010). Interestingly, only the WT and mini-p62 constructs could mediate acidification of tandem tagged KEAP1 when co-expressed as Myc-tagged constructs in the p62 KO HeLa cells. No autophagic turnover of mCherry-YFP-KEAP1, however, was observed upon co-expression with chimera Myc-TFG-p62 or Myc-TFG-minip62 (**Fig. 6G-H, Figure S6A-D**). Autophagy clearance studies established that TFG PB1-p62 chimera can be degraded by autophagy despite their assembly into non-native polymers, whereas these assemblies are not compatible with the structural requirements for mediating degradation of the p62-specific substrate KEAP1.

Discussion

The PB1 domain is a common interaction module present in all kingdoms of life and found in various proteins involved in membrane trafficking, redox regulation, cell division as well as in signaling. In the current study, we focused on the structure in addition to the biological and functional relevance of the p62-PB1 domain in the context of polymeric assemblies. The overall ubiquitin-like fold of the PB1 domain has been determined and different interface types through acidic and basic patches have been identified in earlier studies (Lamark et al., 2003; Wilson et al., 2003). Our cryo-EM structures of filamentous p62

and AtNBR1 PB1 assemblies revealed that the presence of a tandem arginine sequence in the basic motif of type AB interfaces is required to stabilize a polymeric assembly. Although the exact composition of the interface between opposed and electrostatically complementary surfaces is distinctly different for the two PB1 assemblies, the main functional acidic and basic residues including the essential double arginine finger are conserved (**Figure 3**). Furthermore, we observed that the propagation of the helical rung is also distinctly different in p62 and AtNBR1 assemblies, with small changes in primary structure giving rise to large differences in quaternary structure. This property has been characterized in other sequence-related helical systems (Egelman et al., 2015). Interestingly, we also found that the polymeric PB1 domain structures of human p62 and AtNBR1 are assembled from a common helical rung into two morphologically distinct organization types, i.e. in the form of differently organized helical rungs. We speculate that this observed plasticity of assembling a common helical rung is a consequence of flexibility in forming the longitudinal PB1-PB1 interactions in the loop regions. As the constructs used here for structure determination and cellular assays were limited to PB1 domains of AtNBR1 and p62, the relevance and functional consequences of these different morphological arrangements within cellular polymeric assemblies remain open. Full-length p62 was shown to be flexible and at this stage too disordered to be amenable to 3D reconstructions (Ciuffa et al., 2015). In line with our previous analysis, the PB1 domain directs the C-terminus either to the outside or the inside of the helical assembly, depending on the exact helical arrangement. It is possible to envision that different morphological arrangements affect the availability of critical interaction motifs outside the PB1 domain, i.e. LIR and KIR motif as well as the UBA domain.

Previous studies showed that purified full-length p62 can also form helical filaments (Ciuffa et al., 2015; Paine et al., 2005). The existence of these assembly structures inside of cells, however, had not been demonstrated. Therefore, we used the CLEM technique to identify and visualize the ultrastructural organization of p62 found in large clusters known as p62 bodies.

Image analysis confirmed that p62 bodies consist of a meshwork of short filamentous structures. The principal dimension of the observed structures is consistent in width and length with previous measurements *in vitro* (Ciuffa et al., 2015). The structures are compatible with recently observed aggregates of p62 in brain neurons and neuroepithelial cells (Sukseree et al., 2018). Due to the limited length and flexibility, p62 filaments pack loosely into a spheroid-shaped, meshwork-like superstructure. The observed bodies with average dimensions below micrometers in size aggregate in structures that appear morphologically separated from the cytosol (**Figure 4**), suggestive of phase separation as observed previously in reconstitution experiments (Sun et al., 2018; Zaffagnini et al., 2018). The observed body structures of hundreds of nanometers are also significantly larger than individual filaments with on average 30 nm length. When organized in such large superstructures, p62 bodies are more similar in dimension to typical molecular cargo, such as protein aggregates, viruses and organelles when compared with receptor oligomers or filament assemblies alone.

The organization of p62 in filamentous assemblies has direct functional consequences for the interaction with a series of binding partners in the context of autophagy as well as signaling. It has been demonstrated that a polymeric organization of p62 can enhance low affinity interactions to highly avid interactions (Wurzer et al., 2015). In addition, using p62-interacting PB1 domains from MEK5, PKCζ and MEKK3 kinases we show that p62 polymeric assemblies can be capped on one end or dissociate into smaller, ring-like structures. The intact p62 filaments occlude the bulk of PB1 interaction sites that are accessible in its monomeric state (**Figure 6**) (Wilson et al., 2003). Conversely, we show that end-binding of NBR1 to p62 filaments leads to disassembly and shortening, which can thereby modulate the length of the filamentous structure. As NBR1 binding has been shown to promote p62 body formation *in vitro* (Sun et al., 2018; Zaffagnini et al., 2018) to co-localize with p62 bodies *in vivo* (Kirkin et al., 2009), we hypothesize that this filament-end interaction by NBR1 cross-links shorter filaments more effectively into larger

structures and thereby also affects the size of p62 bodies in cells. We speculate that other interactors have similar effects on the size and dynamics of p62 bodies as they may occur in phase separation processes. The size of bodies will also control the availability of interaction sites. The here presented structures and interaction studies of PB1-p62 filaments reveal a series of regulation mechanisms that are critical in the functional context of p62's action in autophagy and signaling.

In order to understand how the assembly state, the specific symmetry and subunit arrangement of this state affect p62's biological function, we tested a series of chimera variants of p62 for their efficiency with regard to cargo uptake and autophagic degradation in the cell. The experiments showed that polymeric as well as oligomeric ring-like scaffolds from related PB1 domains fused to the C-terminal functional domains of p62 can be taken up by the autophagy machinery almost as efficiently as WT-p62. Interestingly, this is not the case for variants of p62 that are monomeric and diffuse in the cytosol (Itakura and Mizushima, 2011). Our results suggest that structures organized in larger oligomeric clusters are sufficient to mediate self-disposal of p62 (**Figure 5**), presumably due to increased avidity of accessible LIR motifs and UBA domains. The specific uptake of the model cargo KEAP1, however, could only be accomplished by WT-p62 and mini-p62 retaining the structural context of native p62 assemblies. Other TFG-PB1-p62 chimera polymers were not capable of transferring KEAP1 to the lysosome. This finding suggests that the PB1-scaffolded p62 polymers also provide critical 3D interfaces that are topologically distinct from the KIR motif and participate in the recognition process of KEAP1 cargo. In conclusion, larger p62 assemblies including ring-like structures and filaments are essential for disposal of autophagy cargo. The precise structural context within the filament assembly is required for specific cargo recognition of KEAP1, and possibly other p62-specific cargoes.

Methods

Protein purification and biophysical characterization

Protein purification. AtNBR1 residues 1-95 (NBR1-PB1), p62 residues 1-122 (p62-PB1) and TFG-1 residues 1-95 (TFG1-PB1) were cloned into a pETM44 expression vector containing a N-terminal His_6-tag, followed by a maltose-binding protein (MBP) tag and a recognition sequence for 3C protease. Proteins were expressed in *E. coli* BL21 (DE3) using auto-induction in lactose-containing media (Studier, 2005). After 18 h, cells were harvested by centrifugation, re-suspended in lysis buffer (50 mM HEPES pH 8.0, 0.5 M NaCl, 0.05 mM TCEP, 0.1 % (v/v) Triton X-100) and lysed by three cycles of rapid freeze-thawing in liquid nitrogen. After removal of cell debris by centrifugation, recombinant proteins were purified by Ni-NTA affinity chromatography, and diafiltrated into 50 mM HEPES pH 7.5, 0.1 M NaCl, 0.05 mM TCEP) followed by proteolytic cleavage of the His_6/MBP by incubation with 1:200 mol/mol 3C protease at ambient temperature. After 1h, the cleavage solution was incubated with Talon resin (Clontech) for 15 min and the resin subsequently sedimented by centrifugation. The supernatant contained the respective PB1 domains in high purity. p62 residues 1-122 (p62-PB1) were cloned into pOPTM and expressed as an MBP fusion protein in *E. coli* BL21 (DE3) using auto-induction (Studier 2005). NBR1 residues 1-85 (NBR1-PB1), pKCζ residues 11-101 (pKCζ-PB1), MEK5 residues 5-108 (MEK5-PB1) and MEKK3 residues 43-127 (MEKK3-PB1) were cloned into the pETM11 containing an N-terminal His_6-tag followed by a recognition sequence for TEV protease. Proteins were expressed in *E. coli* BL21 (DE3) using auto-induction (Studier 2005). For the gold labeling experiments the His_6-tag was not removed to allow binding of 5 nm Ni-NTA-Nanogold® (Nanoprobes). For consistency the His_6-tag was also kept on the proteins for the co-pelletation assay.

Thermal unfolding assays. For thermal denaturation assays protein was dialyzed into 15 mM HEPES (pH 7.5), 150 mM NaCl for pH screening or 100 mM HEPES (pH 7.5) for ionic strength screening. All additives were dissolved in 50 mM HEPES (pH 7.5). A volume of 12.5 µl of a solution containing 500 ng protein was diluted in H_2O with 5× Sypro Orange (Sigma-Aldrich) and

458 immediately mixed with an equal volume of assay condition. All conditions were
459 assessed in triplicate. Fluorescence increase was monitored on a MyiQ real-
460 time PCR instrument (BioRad). Assays were performed over a temperature
461 range of 15–90 °C using a ramp rate of 1 °C/min in steps of 0.5 °C.
462 Fluorescence data from triplicate measurements were baseline corrected
463 individually, and unfolding curves were normalized to maximum fluorescence
464 to give fractional denaturation curves. The apparent T_m was determined as the
465 inflection point of a sigmoidal fit to the normalized fluorescence signal using a
466 customized routine in R.
467
468 **Quantification of PB1 binding affinities**
469 Isothermal titration calorimetry (ITC) experiments were carried out with a VP-
470 ITC system (MicroCal). Experiments were performed at 25 °C in 10 mM HEPES
471 (pH 7.5), 150 mM NaCl. Purified $p62^{1-122}$ D69A/D73A was placed in the reaction
472 cell at a concentration of 5–20 µM with either MEK5 or NBR1 at a concentration
473 of 25–100 µM in the injection syringe. Injections of 10 µL of syringe solution
474 were performed at 4-min intervals. Integration of raw thermogram data,
475 baseline correction and data processing were performed with the NITPIC
476 (Scheuermann and Brautigam, 2015) and SEDPHAT (Zhao et al., 2015)
477 software packages. The data were corrected by the heat of injection calculated
478 from the basal heat remaining after saturation. A one-site binding mode was
479 used to fit the data using a nonlinear least squares algorithm (Brautigam et al.,
480 2016). The values reported are the mean of three independent measurements
481 and errors represent the corresponding standard deviation.

482 **Co-pelleting assay**
483 Co-pelleting assay was performed according to the F-actin binding co-
484 sedimentation assay from Cytoskeleton Inc. In brief, p62-$PB1^{1-122}$, potential
485 binding partner, or p62-$PB1^{1-122}$ together with potential binding partner were
486 incubated for 1 h on ice followed by centrifugation at 49,000 g, 4 °C for 30 min
487 in a TLA-100 rotor. The pellet and supernatant were assayed by SDS-PAGE
488 and stained with Coomassie.

Negative staining EM and filament length measurements

p62-PB1$^{1-122}$ was incubated with different binding partners for 1 h on ice followed by 30 min incubation with 5 nm Ni-NTA-Nanogold® (diluted 1:25). Excess nanogold was removed through pelletation of filaments by ultracentrifugation at 49,000 g, 4 °C for 30 min in a TLA-100 rotor, and the pellet fraction was resuspended in 20 mM HEPES pH 8, 50 mM NaCl. The sample (3.6 µl) was applied to a glow-discharged carbon-coated EM grid and blotted according to the side blotting method (Ohi et al., 2004). Grids were imaged using a Morgagni 268 transmission electron microscope (FEI) operated at 100 kV with a side-mounted 1K CCD camera. Filament length for p62-PB1$^{1-122}$ and p62-PB1$^{1-122}$/HsNBR1$^{1-85}$ were measured using Fiji (Schindelin et al., 2012) and statistical analysis was done using a two-tailed unpaired t-test with Welch's correction in GraphPad Prism 6.0.

Electron cryo-microscopy and image processing

Microscopy. For AtNBR1$^{1-95}$, a total of 3.0 µl of 0.4 mg/ml AtNBR1-PB1 was applied to glow-discharged C-flat grids (CF-1.2/1.3-2C, 400 mesh holey carbon on copper; Protochips) on a Leica GP2 vitrification robot (Leica, Germany) at 95% humidity and 25 °C. The sample was incubated for 10 s on the grid before blotting for 2 s from the back side of the grid and immediately flash-frozen in liquid ethane. Micrographs were acquired at 300 kV using an FEI Titan Krios (Thermo Fisher Scientific) equipped with a Falcon II direct detector at a magnification of 59,000, corresponding to a pixel size of 1.386 Å at the specimen level. Image acquisition was performed with EPU Software (Thermo Fisher Scientific) and micrographs were collected at an underfocus varying between 0.5 and 4.5 µm. We collected a total of seven frames accumulating to a dose of 14 e^{-}/Å^{-2} over 0.82 sec. In total, 742 micrographs were acquired, of which we selected 684 for further processing after discarding micrographs that did not show Thon rings exceeding 6 Å.

For p62$^{1-122}$, L-type filaments were enriched by the following procedure: 0.2 mg p62-PB1 (100 µl) was ammonium sulfate precipitated (25 % v/v) and incubated o/n at 4 °C. Sample was spun at 17,000 g for 15 min at 4 °C and pellet was resuspended in 50 mM TRIS (pH 7.5), 100 mM NaCl, 4 mM DTT. This

ammonium sulfate precipitation was repeated a second time. In the final step sample was centrifuged at 49,000 g for 45 min at 4 °C and pellet resuspended in 25 µl. A total of 3.6 µl resulting p62-PB1$^{1-122}$ solution was applied to glow-discharged Quantifoil R2/1 Cu 400 mesh grids on a Vitrobot Mark IV (Thermo Fisher Scientific) at 10°C and 100% humidity. The sample was blotted for 5 s from both sides and flash-frozen in liquid ethane after a drain time of 1 s. Micrographs were acquired at 300 kV using a FEI Titan Krios (Thermo Fisher Scientific) with a K2 Summit detector (Gatan, Inc.), a pixel size of 1.04 Å and an underfocus ranging from 0.5 to 2.5 µm. 40 frames were collected in counting mode with a dose rate of 4.5 $e^-/Å^2s$ and a total dose of 40 $e^-/Å^2$. In total, 2277 micrographs were automatically collected and 856 micrographs without ice contamination or carbon chosen for further processing.

Image processing. For the AtNBR1 dataset, movie frames were aligned using MOTIONCORR (Li et al., 2013). The resulting frame stacks and integrated images (total frame sums) were used for further processing. The contrast-transfer function of the micrographs was determined with CTFFIND4 using the integrated images. Helix coordinates were picked using e2helixboxer.py from the EMAN2 package (Tang et al., 2007). Initially a subset of 100 images was selected for preliminary processing in SPRING (Desfosses et al., 2014). Briefly, overlapping helix segments of 350 x 350 Å dimensions were excised from the frame-aligned images with a mean step size of 60 Å using the SEGMENT module in SPRING. In-plane rotated, phase-flipped segments were subjected to 2D classification by k-means clustering as implemented in SPARX (Hohn et al., 2007). During a total of five iterations, the segments were classified and iteratively aligned against a subset of class averages chosen based on the quality of their power spectra. Class averages revealed two distinct helix types referred to as S-type and L-type. We determined the helical symmetry for the L-type helices by indexing of the power spectra obtained from the 2D classification. Final symmetry parameters were determined with a symmetry search grid using SEGMENTREFINE3DGRID. For 3D refinement and reconstruction, the excised segments were convolved with the CTF and no in-plane rotation was applied prior to reconstruction. Starting from the symmetry

parameters obtained for the L-type helix, symmetry parameters of the S-type helix were refined. The maximum of the mean cross correlation peak between computed and experimental power spectra was found at a pitch of 70 Å, 11.55 units per turn for the two-start L-type helix and a pitch of 68.2 Å, 11.55 units per turn for the one-start S-type helix. Using the refined symmetry parameters, we performed a competitive high-resolution multi-model structure refinement using all 684 images with a final resolution of 4.5/3.9 Å and 5.0/4.4 Å (FSC 0.5/0.143) for the two-start (L-type) and one-start (S-type) helix reconstructions (**Table S2**).

For the p62$^{1\text{-}122}$ dataset, movie frames were aligned in RELION3 (Zivanov et al, 2018) using 5x5 patches. The contrast-transfer function of the micrographs was determined with Gctf (Zhang, 2016). Helix coordinates were automatically picked in RELION3 and segments extracted with a step of 22.5 Å, binning 2 and an unbinned box size of 256 pixels. 2D classification with 100 classes was performed and classes were selected that showed secondary structure features. Two separate subsequent 2D classifications were performed with two distinct groups of 2D classes belonging to an S-type and L-type pattern. Using SEGCLASSRECONSTRUCT from the SPRING package (Desfosses et al., 2014) a series of putative helical symmetry solutions could be obtained. In addition to running a series of refinements with these symmetry solutions, a C1 reconstruction provided additional hints for symmetry parameters. Imposition of wrong symmetry parameters led to smeared density features whereas only the correct symmetries for both filament types led to recognizable high-resolution side-chain features. Helical symmetry was automatically refined in RELION to 77.3º helical rotation and 4.8 Å rise for the S-type and 26.5º rotation and 9.8 Å rise for the L-type, respectively (**Table S2**). Focussed refinement was performed using a mask covering the central 25% of the filament along the helical axis. This approach improved the resulting resolution for the L-type, but not for the S-type. Final resolution was estimated at 3.5 Å and 4.0 Å using the FSC and the 0.143 criterion cutoff (Rosenthal and Henderson, 2003), for the L and S-type respectively.

585 **Post-processing and model building**. For visual display and model building,
586 the AtNBR1 EM density map of the individual reconstructions were initially
587 filtered to 3.9 Å and 4.4 Å respectively and sharpened using a B-factor of -200
588 $Å^2$. The AtNBR1-PB1 subunit model was built into the 3.9 Å density map of the
589 L-type arrangement *de novo* in COOT (Emsley and Cowtan, 2004). Residues
590 81-85 could not be built *de novo* due to weak density, but were added based
591 on the high-resolution crystal structure obtained in this study which showed
592 good agreement with the weak density. For the p62-PB1 (3-102) map, the NMR
593 structure from *rattus norvegicus* (PDB ID 2kkc) was rigid-body fitted into the
594 RELION-postprocessed density of the L-type filament and then manually
595 adjusted to the human sequence in COOT (Emsley and Cowtan, 2004). The
596 models were expanded using helical symmetry and a nine-subunit segment
597 was excised to serve as a refinement target taking into account interactions
598 along the azimuthal propagation and lateral interactions along the helical axis.
599 Following real-space refinement in PHENIX (Adams et al., 2010), we used
600 model-based density scaling (Jakobi et al., 2017) to generate locally sharpened
601 maps and completed the model in COOT followed by further iterations of real-
602 space refinement. The final monomer atomic model from the L-type
603 arrangement was rigid-body fitted into the S-type density and refinement of the
604 model was performed as described above.

605 **X-ray crystallography**
606 Crystals of $AtNBR1^{1-95}$ carrying a D60A/D62A mutation were grown using
607 hanging drop vapour diffusion at 292 K by mixing equal volumes of 11 mg ml^{-1}
608 protein and reservoir solution. Within 10 h, crystals appeared as needle clusters
609 in 0.085 M MES (pH 6.5), 18.2% (w/v) PEG20000. Isolated needles (10×2×4
610 µm) were obtained by streak seeding with a cat whisker into 0.1 M MES (pH
611 6.5), 18-20% (w/v) PEG20000 or 0.1 M sodium cacodylate (pH 6.5), 0.2 M
612 $(NH_4)_2SO_4$, 30-33% PEG8000. For cryo-protection, crystals were soaked in the
613 crystallization condition supplemented with 15% (v/v) glycerol. Diffraction data
614 were collected on the ID23-2 microfocus beamline at the European Synchrotron
615 Radiation Facility (ESRF) and processed with XDS (Kabsch, 2010) (Kabsch,
616 1993) and AIMLESS (Evans and Murshudov, 2013). Initial attempts to solve

the crystal structure using the cryo-EM atomic model were unsuccessful. The crystal structure was solved using molecular replacement using the monomer density from the L-type cryo-EM reconstruction as the search model. Briefly, the monomer density was obtained by cutting out density extending 4.5 Å beyond the atomic coordinates. The extracted map segment was centred in a P1 unit cell extending over three times the maximum map dimension, converted to structure factors using a in house, customized CCTBX (Grosse-Kunstleve et al., 2002) routine and used for automated molecular replacement in PHASER (Mccoy et al., 2007). The top scoring solution had a translation function Z-score of 16.5. Henderson-Lattmann coefficients were generated from the figure-of-merit (FOM) obtained from the PHASER solution and employed for phase extension using the high-resolution X-ray crystallographic data by density modification in RESOLVE (Terwilliger et al., 2013), yielding excellent electron density. Using the 1.9 Å data, the model was built using Arp/Warp (Langer et al., 2008) and completed manually in COOT. Table 1 summarizes data collection and refinement statistics.

Correlative light and electron microscopy

For CLEM, RPE1 cells were transiently transfected with pDestEGFP-NBR1(D50R) (Kirkin et al., 2009) and grown on photo-etched coverslips (Electron Microscopy Sciences, Hatfield, USA). Cells were fixed in 4% formaldehyde, 0.1% glutaraldehyde/0.1 M PHEM (240 mM PIPES, 100 mM HEPES, 8 mM $MgCl_2$, 40 mM EGTA, pH 6.9), for 1h. The coverslips were then washed in PBS containing 0.005% saponin and stained with the indicated primary antibodies for 1 hour (rabbit anti-p62 (MBL, PM045), mouse anti-NBR1 (Santa Cruz, #sc-130380)), washed three times in PBS/saponin, stained with secondary antibodies (from Jackson ImmunoResearch Laboratories) for 1 hour, washed three times in PBS and shortly rinsed in water. The cells were mounted with Mowiol containing 2 μg/ml Hoechst 33342 (Sigma-Aldrich). Mounted coverslips were examined with a Zeiss LSM780 confocal microscope (Carl Zeiss MicroImaging GmbH, Jena, Germany) utilizing a Laser diode 405-30 CW (405 nm), an Ar-Laser Multiline (458/488/514 nm), a DPSS-561 10 (561 nm), and a HeNe-laser (633 nm). The objective used for confocal microscopy

649 was a Zeiss plan-Apochromat 63x/1.4 Oil DIC III. Cells of interest were
650 identified by fluorescence microscopy and a Z-stack was acquired. The relative
651 positioning of the cells on the photo-etched coverslips was determined by
652 taking a DIC image. The coverslips were removed from the object glass,
653 washed with 0.1 M PHEM buffer and fixed in 2 % glutaraldehyde/0.1 M PHEM
654 for 1h. Cells were postfixed in osmium tetroxide, stained with tannic acid,
655 dehydrated stepwise to 100 % ethanol and flat-embedded in Epon. Serial
656 sections (~100-200 nm) were cut on an Ultracut UCT ultramicrotome (Leica,
657 Germany), collected on formvar coated mesh-grids, and poststained with lead
658 citrate.

659 **Electron tomography from cellular sections**
660 Samples were observed using a FEI Talos F200C electron microscope
661 (Thermo Fisher Scientific, Netherlands). Image series were taken between -60°
662 and 60° with 2° increment. Single-tilt or double-tilt series (as indicated in the
663 text above) were recorded with a Ceta 16M camera. Single axis tomograms
664 were computed using weighted back projection and, when applicable, merged
665 into a dual-axis tomogram using the IMOD package. Display and animation of
666 segmentation of tomograms were performed using a scripted workflow in
667 ImageJ and IMARIS.

668 **Autophagy and p62 turnover assays**
669 **Antibodies and reagents.** The following antibodies were used: mouse anti-
670 Myc antibody (Cell Signaling, Cat.#2276#, 1:8000 for western blots and 1:5000
671 for confocal imaging); rabbit anti-GFP antibody (Abcam, ab290, 1:5000);
672 guinea pig anti-p62 antibody (Progen, Cat#Gp62-C#, 1:5000); rabbit anti-Actin
673 antibody (Sigma, Cat#A2066#, 1:1000); Alexa Fluor® 647-conjugated goat
674 anti-mouse IgG (A21236, 1:1000); HRP-conjugated goat anti-mouse IgG
675 (1:5000), goat anti rabbit IgG (1:5000) and goat anti-guinea pig IgG (1:5000).
676
677 **Generation of HeLa cells KO for p62 by CRISPR/Cas9.** To generate
678 CRISPR/Cas9 p62 gRNA plasmid, sense and antisense p62 gRNA were
679 annealed and then inserted into plasmid pX330 (Ref PMID: 23287718). For

680 generation of CRISPR/Cas9 p62 KO cells, approximately 30,000 HeLa cells
681 were seeded per well into 24 well plates and transfected with plasmid pX330
682 p62 gRNA using Metafectene Pro (Biontex T040). For clonal selection, cells
683 were treated with 500 ng/ml of puromycin 24 hours after transfection for 48-72
684 hours. Later, single cells were sorted into 96 well plate using FACS
685 (fluorescence-activated cell sorting). These clones were allowed to grow for 7-
686 10 days before screening for KO using immunoblotting. The following sense 5'-
687 CACCGTCATCCTTCACGTAGGACA-3' and antisense 5'-
688 AAACTGTCCTACGTGAAGGATGAC-3' gRNAs were used.
689
690 **Construction of Plasmids.** The gateway entry clone pENTR-p62 has been
691 described previously (Lamark et al., 2003). pENTR-p62 Δ123-319 was made
692 by deletion of pENTR-p62. TFG-p62 fusion constructs were produced by
693 InFusion PCR. To subclone the TFG-p62 fusion constructs into an ENTRY
694 vector, an NcoI site was inserted into the start codon of p62 in pENTR-p62,
695 creating pENTR-p62$_{CCATGG}$. The start codons in TFG-p62 (AJD152) and TFG-
696 mini-p62 (AJD157) already have NcoI sites, and there is an additional NcoI site
697 close to the end of the p62 cDNA sequence in pENTR-p62, TFG-p62 and TFG-
698 mini-p62. To replace wild type p62 of pENTR-p62$_{CCATGG}$, TFG-p62 from
699 AJD152 and AJD157 were subcloned as NcoI fragments into pENTR-
700 p62CCATGG cut with NcoI, creating pENTR-TFG-p62 and pENTR-TFG-mini-
701 p62, respectively. Gateway LR recombination reactions were performed as
702 described in the Gateway cloning technology instruction manual (Invitrogen).
703 Gateway expression clones pDest-Myc-p62, pDest-EGFP-p62 and pDest-
704 mCherry-EGFP-KEAP1 have been described previously (Jain et al., 2010;
705 Lamark et al., 2003). pDest-Myc-p62 Δ123-319, pDest-Myc- TFG-p62 and
706 pDest-Myc- TFG-mini-p62 were made by Gateway LR reactions using
707 destination vector pDest-Myc (Lamark et al., 2003; mammalian expression of
708 N-terminal Myc-tagged proteins). pDest-EGFP-p62 Δ123-319, pDest-EGFP-
709 TFG-p62 and pDest-EGFP-TFG-mini-p62 were made using destination vector
710 pDest-EGFP-C1 (Lamark et al., 2003; mammalian expression of N-terminal
711 EGFP-tagged proteins). pDest-mCherry-EYFP-p62, pDest-mCherry-EYFP-

712 p62 Δ123-319, pDest-mCherry-EYFP- TFG-p62 and pDest-mCherry-EYFP-
713 TFG-mini-p62 were made using destination vector pDest-mCherry-EYFP
714 (Bhujabal et al., 2017; mammalian expression of N-terminal mCherry-EYFP
715 double tagged proteins).
716
717 **Cell culture and transfections.** HeLa p62 KO cells were cultured in Eagle's
718 minimum essential medium with 10 % fetal bovine serum (Biochrom AG,
719 S0615), non-essential amino acids, 2 mM L-glutamine and 1 % streptomycin-
720 penicillin (Sigma, P4333). For transfection was used the same media but
721 without 1% streptomycin-penicillin. Cells were fixed in 4 % PFA for 20 min at
722 room temperature. For immunostaining, cells were permeabilized with cold
723 methanol for 5 min at room temperature, blocked in 3 % goat serum/PBS and
724 incubated at room temperature with antibodies. For DNA staining was used
725 1:4000 dilution in PBS of DAPI (Thermo Scientific; pr.66248). Samples were
726 mounted using Mowiol 4-88 (Calbiochem 475904). Cells were examined using
727 a Zeiss LSM780 microscope with a 63 x 1.4 oil-objective or a Leica TCS SP8
728 confocal microscope, 40 X 1.3 oil-objective.
729
730 **Western blot analyses.** Transfected HeLa p62 KO cells were harvested in 50
731 mM Tris pH 7.4, 2 % SDS, 1 % glycerol. Cell lysates were cleared by
732 centrifugation, and supernatants resolved by SDS-PAGE and transferred to
733 Hybond-ECL nitrocellulose membrane (GE healthcare). The membrane was
734 blocked with 5 % nonfat dry milk in PBS-T, incubated with primary antibody
735 overnight and HRP-conjugated secondary antibody for 1 hour at room
736 temperature. Proteins were detected by immunoblotting with a
737 chemiluminescence Luminol kit (SC-2048, Santa Cruz Biotechnology) using a
738 LumiAnalyst Imager (Roche Applied Sciences).
739

740 **Accession numbers**
741 The PDB accession number for the atomic coordinates and structure factors for
742 the AtNBR1-PB1 X-ray crystal structure reported in this paper is PDB-xxx. The
743 EMDB accession numbers for the L- and S-type AtNBR1-PB1 cryo-EM maps

and models are EMD-xxx/EMD-yyy, and PDB-xxx/PDB-yyy and those for the L- and S-type p62-PB1 cryo-EM maps and atomic coordinate models are EMD-xxx/EMD-yyy and PDB-xxx/PDB-yyy, respectively.

Acknowledgements

We thank the European Synchrotron Radiation Facility (ESRF, Grenoble, France), the EMBL beamlines at PETRA-III (DESY, Hamburg, Germany) and the beamline scientists at ESRF ID23-2 and EMBL-DESY P14 for excellent support. The project was financially supported by the Boehringer Ingelheim Fund's Exploration Grant. AJJ acknowledges financial support by an EMBL Interdisciplinary Postdoc (EIPOD) fellowship under Marie Curie Actions (PCOFUND-GA-2008-229597), a Marie Sklodowska-Curie IEF fellowship (PIEF-GA-2012-331285), the Deutsche Forschungsgemeinschaft (DFG) through the excellence cluster "The Hamburg Center for Ultrafast Imaging (CUI) – Structure, Dynamics and Control of Matter at the Atomic Scale" (EXC1074) and the Joachim Herz Foundation.

Competing interests

The authors declare no financial or non-financial competing interest.

References

Adams, P.D., Afonine, P.V., Bunkóczi, G., Chen, V.B., Davis, I.W., Echols, N., Headd, J.J., Hung, L.-W., Kapral, G.J., Grosse-Kunstleve, R.W., et al. (2010). PHENIX: a comprehensive Python-based system for macromolecular structure solution. Acta Crystallogr D Biol Crystallogr *66*, 213–221.

Bjørkøy, G., Lamark, T., Brech, A., Outzen, H., Perander, M., Øvervatn, A., Stenmark, H., and Johansen, T. (2005). p62/SQSTM1 forms protein aggregates degraded by autophagy and has a protective effect on huntingtin-induced cell death. The Journal of Cell Biology *171*, 603–614.

Brautigam, C.A., Zhao, H., Vargas, C., Keller, S., and Schuck, P. (2016). Integration and global analysis of isothermal titration calorimetry data for studying macromolecular interactions. Nature Protocols *11*, 882–894.

Britzen-Laurent, N., Bauer, M., Berton, V., Fischer, N., Syguda, A., Reipschläger, S., Naschberger, E., Herrmann, C., and Stürzl, M. (2010).

777 Intracellular trafficking of guanylate-binding proteins is regulated by
778 heterodimerization in a hierarchical manner. PLoS ONE *5*, e14246.

779 Carroll, B., Otten, E.G., Manni, D., Stefanatos, R., Menzies, F.M., Smith, G.R.,
780 Jurk, D., Kenneth, N., Wilkinson, S., Passos, J.F., et al. (2018). Oxidation of
781 SQSTM1/p62 mediates the link between redox state and protein homeostasis.
782 Nature Communications *9*, 256.

783 Cheng, Y. (2015). Single-Particle Cryo-EM at Crystallographic Resolution.
784 Cell *161*, 450–457.

785 Ciuffa, R., Lamark, T., Tarafder, A.K., Guesdon, A., Rybina, S., Hagen,
786 W.J.H., Johansen, T., and Sachse, C. (2015). The Selective Autophagy
787 Receptor p62 Forms a Flexible Filamentous Helical Scaffold. Cell Reports.

788 Desfosses, A., Ciuffa, R., Gutsche, I., and Sachse, C. (2014). SPRING - An
789 image processing package for single-particle based helical reconstruction
790 from electron cryomicrographs. J Struct Biol *185*, 15–26.

791 Duran, A., Linares, J.F., Galvez, A.S., Wikenheiser, K., Flores, J.M., Diaz-
792 Meco, M.T., and Moscat, J. (2008). The signaling adaptor p62 is an important
793 NF-kappaB mediator in tumorigenesis. Cancer Cell *13*, 343–354.

794 Egelman, E.H., Xu, C., DiMaio, F., Magnotti, E., Modlin, C., Yu, X., Wright, E.,
795 Baker, D., and Conticello, V.P. (2015). Structural plasticity of helical
796 nanotubes based on coiled-coil assemblies. Structure *23*, 280–289.

797 Emsley, P., and Cowtan, K. (2004). Coot: model-building tools for molecular
798 graphics. Acta Crystallogr D Biol Crystallogr *60*, 2126–2132.

799 Evans, P.R., and Murshudov, G.N. (2013). How good are my data and what is
800 the resolution? Acta Crystallogr D Biol Crystallogr *69*, 1204–1214.

801 Grosse-Kunstleve, R.W., Sauter, N.K., Moriarty, N.W., and Adams, P.D.
802 (2002). The Computational Crystallography Toolbox: crystallographic
803 algorithms in a reusable software framework. J Appl Crystallogr *35*, 126–136.

804 Hohn, M., Tang, G., Goodyear, G., Baldwin, P.R., Huang, Z., Penczek, P.A.,
805 Yang, C., Glaeser, R.M., Adams, P.D., and Ludtke, S.J. (2007). SPARX, a
806 new environment for Cryo-EM image processing. J Struct Biol *157*, 47–55.

807 Itakura, E., and Mizushima, N. (2011). p62 Targeting to the autophagosome
808 formation site requires self-oligomerization but not LC3 binding. The Journal
809 of Cell Biology *192*, 17–27.

810 Jain, A., Lamark, T., Sjøttem, E., Larsen, K.B., Awuh, J.A., Øvervatn, A.,
811 McMahon, M., Hayes, J.D., and Johansen, T. (2010). p62/SQSTM1 is a target
812 gene for transcription factor NRF2 and creates a positive feedback loop by
813 inducing antioxidant response element-driven gene transcription. J Biol Chem
814 *285*, 22576–22591.

815 Jakobi, A.J., Wilmanns, M., and Sachse, C. (2017). Model-based local density
816 sharpening of cryo-EM maps. Elife *6*, e27131.

817 Johansen, T., and Lamark, T. (2011). Selective autophagy mediated by
818 autophagic adapter proteins. Autophagy *7*, 279–296.

819 Kabsch, W. (1993). Automatic processing of rotation diffraction data from
820 crystals of initially unknown symmetry and cell constants - Kabsch - 2007 -
821 Journal of Applied Crystallography - Wiley Online Library. J Appl Crystallogr
822 *26*, 795–800.

823 Kabsch, W. (2010). Integration, scaling, space-group assignment and post-
824 refinement. Acta Crystallogr D Biol Crystallogr *66*, 133–144.

825 Katsuragi Y, Ichimura Y, Komatsu M. (2015) p62/SQSTM1 functions as a
826 signaling hub and an autophagy adaptor. FEBS J *282*, 4672–4678

827 Kirkin, V., Lamark, T., Sou, Y.-S., Bjørkøy, G., Nunn, J.L., Bruun, J.-A.,
828 Shvets, E., McEwan, D.G., Clausen, T.H., Wild, P., et al. (2009). A role for
829 NBR1 in autophagosomal degradation of ubiquitinated substrates. Mol Cell
830 *33*, 505–516.

831 Korasick DA, Westfall CS, Lee SG, Nanao MH, Dumas R, Hagen G, Guilfoyle
832 TJ, Jez JM, Strader LC. (2014) Proc Natl Acad Sci U S A *111*, 5427-5432.

833 Kraft, C., Peter, M., and Hofmann, K. (2010). Selective autophagy: ubiquitin-
834 mediated recognition and beyond. Nat Cell Biol *12*, 836–841.

835 Lamark, T., Perander, M., Outzen, H., Kristiansen, K., Øvervatn, A.,
836 Michaelsen, E., Bjørkøy, G., and Johansen, T. (2003). Interaction codes
837 within the family of mammalian Phox and Bem1p domain-containing proteins.
838 J Biol Chem *278*, 34568–34581.

839 Langer, G., Cohen, S.X., Lamzin, V.S., and Perrakis, A. (2008). Automated
840 macromolecular model building for X-ray crystallography using ARP/wARP
841 version 7. Nature Protocols *3*, 1171–1179.

842 Li, X., Mooney, P., Zheng, S., Booth, C.R., Braunfeld, M.B., Gubbens, S.,
843 Agard, D.A., and Cheng, Y. (2013). Electron counting and beam-induced
844 motion correction enable near-atomic-resolution single-particle cryo-EM. Nat
845 Meth *10*, 584–590.

846 Mccoy, A.J., Grosse-Kunstleve, R.W., Adams, P.D., Winn, M.D., Storoni, L.C.,
847 and Read, R.J. (2007). Phaser crystallographic software. J Appl Crystallogr
848 *40*, 658–674.

849 Mizushima, N., and Komatsu, M. (2011). Autophagy: renovation of cells and
850 tissues. Cell *147*, 728–741.

851 Moscat, J., Diaz-Meco, M.T., Albert, A., and Campuzano, S. (2006). Cell
852 Signaling and Function Organized by PB1 Domain Interactions. Mol Cell *23*,
853 631–640.

854 Ohi, M., Li, Y., Cheng, Y., and Walz, T. (2004). Negative Staining and Image
855 Classification – Powerful Tools in Modern Electron Microscopy. Biol. Proc.
856 Online *6*, 23–34.

857 Paine, M.G., Babu, J.R., Seibenhener, M.L., and Wooten, M.W. (2005).
858 Evidence for p62 aggregate formation: role in cell survival. FEBS Lett *579*,
859 5029–5034.

860 Pankiv, S., Clausen, T.H., Lamark, T., Brech, A., Bruun, J.A., Outzen, H.,
861 Overvatn, A., Bjørkøy, G., and Johansen, T. (2007). p62/SQSTM1 Binds
862 Directly to Atg8/LC3 to Facilitate Degradation of Ubiquitinated Protein
863 Aggregates by Autophagy. J Biol Chem *282*, 24131–24145.

864 Ren, J., Wang, J., Wang, Z., and Wu, J. (2014). Structural and biochemical
865 insights into the homotypic PB1-PB1 complex between PKCζ and p62. Sci
866 China Life Sci *57*, 69–80.

867 Saio, T., Yokochi, M., and Inagaki, F. (2009). The NMR structure of the p62
868 PB1 domain, a key protein in autophagy and NF-kappaB signaling pathway. J
869 Biomol NMR *45*, 335–341.

870 Saio, T., Yokochi, M., Kumeta, H., and Inagaki, F. (2010). PCS-based
871 structure determination of protein-protein complexes. J Biomol NMR *46*, 271–
872 280.

873 Scheuermann, T.H., and Brautigam, C.A. (2015). High-precision, automated
874 integration of multiple isothermal titration calorimetric thermograms: new
875 features of NITPIC. Methods *76*, 87–98.

876 Schindelin, J., Arganda-Carreras, I., Frise, E., Kaynig, V., Longair, M.,
877 Pietzsch, T., Preibisch, S., Rueden, C., Saalfeld, S., Schmid, B., et al. (2012).
878 Fiji: an open-source platform for biological-image analysis. Nat Meth *9*, 676–
879 682.

880 Studier, F.W. (2005). Protein production by auto-induction in high-density
881 shaking cultures. Protein Expr Purif *41*, 207–234.

882 Sukseree, S., László, L., Gruber, F., Bergmann, S., Narzt, M.S., Nagelreiter,
883 I.M., Höftberger, R., Molnár, K., Rauter, G., Birngruber, T., et al. (2018).
884 Filamentous Aggregation of Sequestosome-1/p62 in Brain Neurons and
885 Neuroepithelial Cells upon Tyr-Cre-Mediated Deletion of the Autophagy Gene
886 Atg7. Mol. Neurobiol. *55*, 8425–8437.

887 Sumimoto, H., Kamakura, S., and Ito, T. (2007). Structure and Function of the
888 PB1 Domain, a Protein Interaction Module Conserved in Animals, Fungi,
889 Amoebas, and Plants. Science Signaling *2007*, re6.

890 Sun, D., Wu, R., Zheng, J., Li, P., and Yu, L. (2018). Polyubiquitin chain-
891 induced p62 phase separation drives autophagic cargo segregation. Cell Res.
892 *28*, 405–415.

893 Svenning, S., Lamark, T., Krause, K., and Johansen, T. (2011). Plant NBR1 is
894 a selective autophagy substrate and a functional hybrid of the mammalian
895 autophagic adapters NBR1 and p62/SQSTM1. Autophagy *7*, 993–1010.

896 Tang, G., Peng, L., Baldwin, P.R., Mann, D.S., Jiang, W., Rees, I., and
897 Ludtke, S.J. (2007). EMAN2: an extensible image processing suite for
898 electron microscopy. J Struct Biol *157*, 38–46.

899 Terwilliger, T.C., Read, R.J., Adams, P.D., Brunger, A.T., Afonine, P.V., and
900 Hung, L.W. (2013). Model morphing and sequence assignment after
901 molecular replacement. Acta Crystallogr D Biol Crystallogr *69*, 2244–2250.

902 Wilson, M.I., Gill, D.J., Perisic, O., Quinn, M.T., and Williams, R.L. (2003).
903 PB1 domain-mediated heterodimerization in NADPH oxidase and signaling
904 complexes of atypical protein kinase C with Par6 and p62. Mol Cell *12*, 39–50.

905 Wurzer, B., Zaffagnini, G., Fracchiolla, D., Turco, E., Abert, C., Romanov, J.,
906 and Martens, S. (2015). Oligomerization of p62 allows for selection of
907 ubiquitinated cargo and isolation membrane during selective autophagy. Elife
908 *4*, 1687.

909 Zaffagnini, G., Savova, A., Danieli, A., Romanov, J., Tremel, S., Ebner, M.,
910 Peterbauer, T., Sztacho, M., Trapannone, R., Tarafder, A.K., et al. (2018).
911 p62 filaments capture and present ubiquitinated cargos for autophagy. Embo
912 J *37*.

913 Zhang, K. (2016). Gctf: Real-time CTF determination and correction. J Struct
914 Biol *193*, 1–12.

915 Zhao, H., Piszczek, G., and Schuck, P. (2015). SEDPHAT--a platform for
916 global ITC analysis and global multi-method analysis of molecular
917 interactions. Methods *76*, 137–148.

918

Figure legends

Figure 1

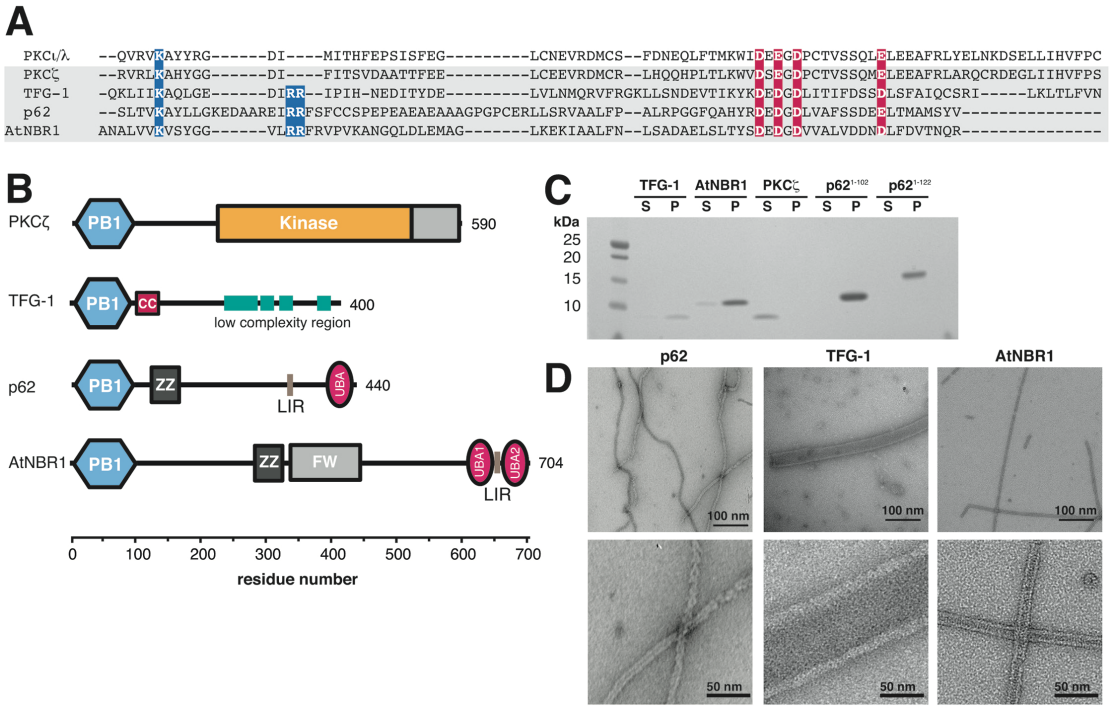

Figure 1. Type A/B PB1 domains and their capability to form polymers. (A) Sequence alignment of the type A/B PB1 domains with highlighted tandem arginine motif. (B) Domain architecture of PKCz, TFG-1, p62, and AtNBR1 proteins. (C) Pelletation assay of purified type A, B or AB PB1 domains: TFG-1, AtNBR1, PKCζ, $p62^{1-102}$ and $p62^{1-122}$. Corresponding lanes of soluble (S) and pellet (P) fraction are shown. Only PKCζ remains soluble whereas TFG-1, AtNBR1 and p62 are found in the pellet. (D) Electron micrographs of negatively stained specimens reveal elongated filamentous $p62^{1-122}$, tubular polymers of TFG-1 and AtNBR1 of 145 ± 5, 900 ± 52 and 120 ± 4 Å nm in diameter, respectively.

Figure 2

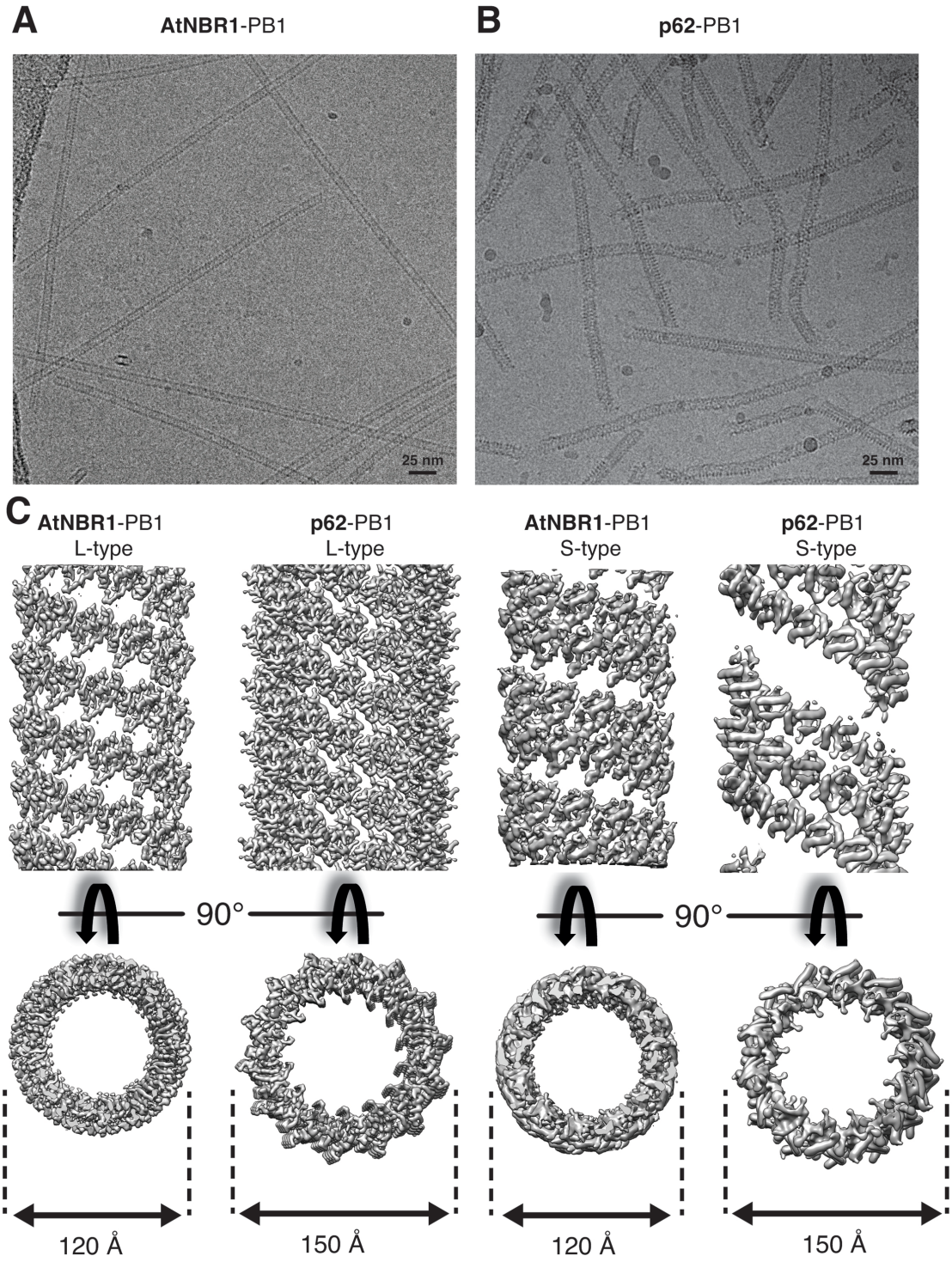

931

932 **Figure 2. Cryo-EM structures of AtNBR1 and p62$^{1-122}$.**

933 (A) Electron cryo-micrograph of AtNBR1-PB1 and (B) p62-PB1$^{1-122}$ assemblies.

934 (C) Side and top views for determined cryo-EM structures of L-type AtNBR1-

935 PB1 (far left), p62-PB1 (left) and S-type assembly of AtNbr-PB1 (right), p62-

936 PB1 (far right).

Figure 3

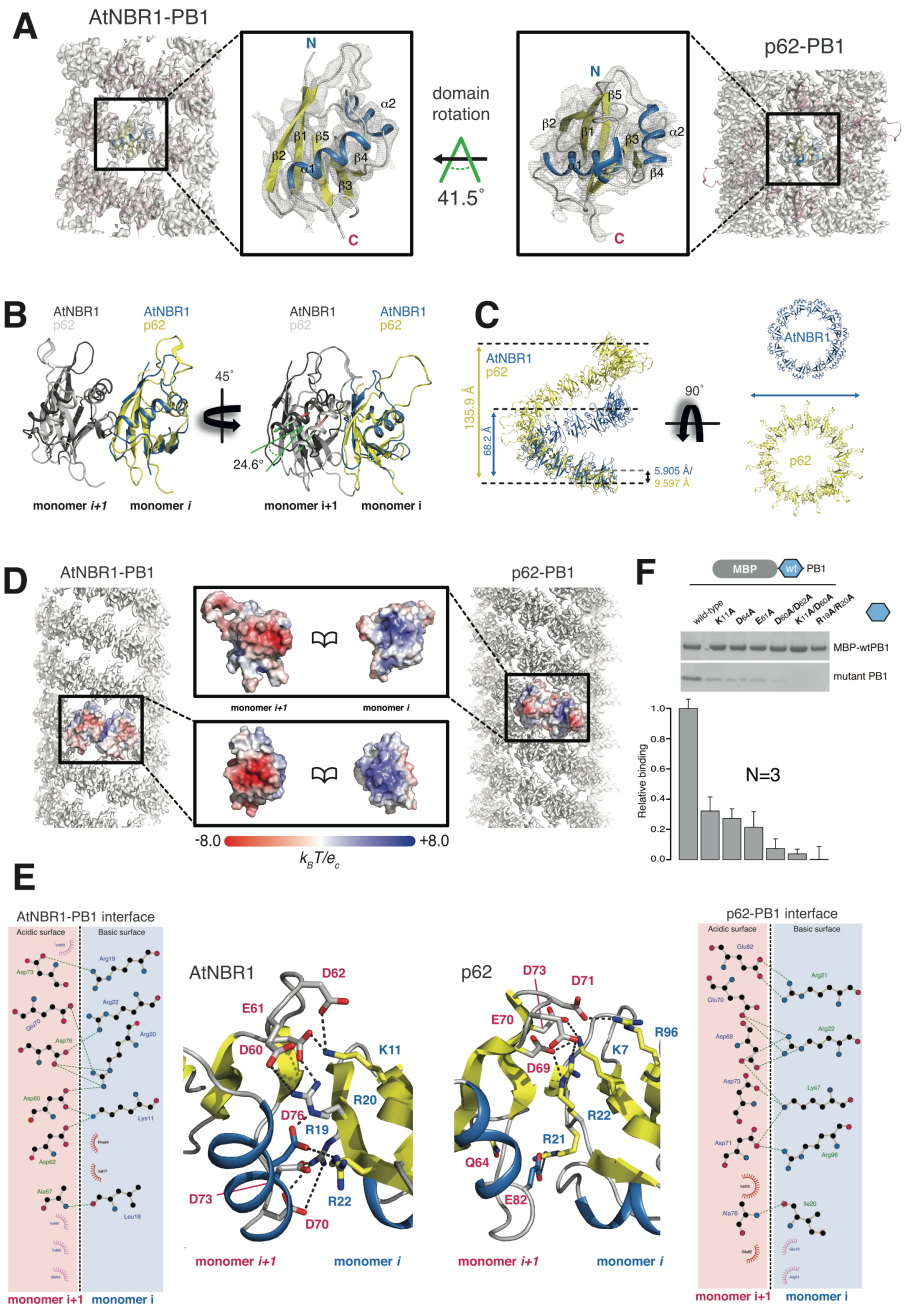

Figure 3. Structural basis of PB1 polymer formation.

(A) Cryo-EM density maps of AtNBR1-PB1 (left) and p62-PB1 filaments are shown with atomic models superposed on the density. Close-ups show that both PB1 domains display the canonical ubiquitin-like fold (center left and center right). The arrow indicates the rotation of the p62-PB1 subunit relative to the AtNBR1-PB1 subunit in their respective assemblies. (B, C) Differences in the PB1-PB1 interface give rise to different helical architectures. (Left) Monomer *i* of AtNBR1 (blue) and monomer *i* p62 (yellow) were superposed to

946 visualize the degree of domain rotation towards the next monomer along the
947 helical rung (monomer i+1). (Right) Adjacent subunits along the helical rung for
948 AtNBR1 display a 25° inward rotation compared with adjacent subunits of p62,
949 explaining the observed differences in helical symmetry and diameter of
950 AtNBR1-PB1 and p62-PB1 filaments, respectively (C).
951 (D) Electrostatic potential surface of the determined AtNBR1-PB1 and p62-PB1
952 structures. For both structures, the propagation of the helical structure is
953 mediated and stabilized by positively and negatively charged surfaces on
954 opposite faces of the PB1 fold. (E) Schematic illustration and detailed
955 interactions of the PB1-PB1 interface as determined from the AtNBR1-PB1 and
956 p62-PB1 cryo-EM structures, respectively. The structures are shown in cartoon
957 representation highlighting key electrostatic residue contacts shown as sticks.
958 (F) *In vitro* pulldown with maltose-binding protein (MBP)-tagged wild-type
959 AtNBR1-PB1 of structure-based AtNBR1-PB1 domain mutants.

Figure 4

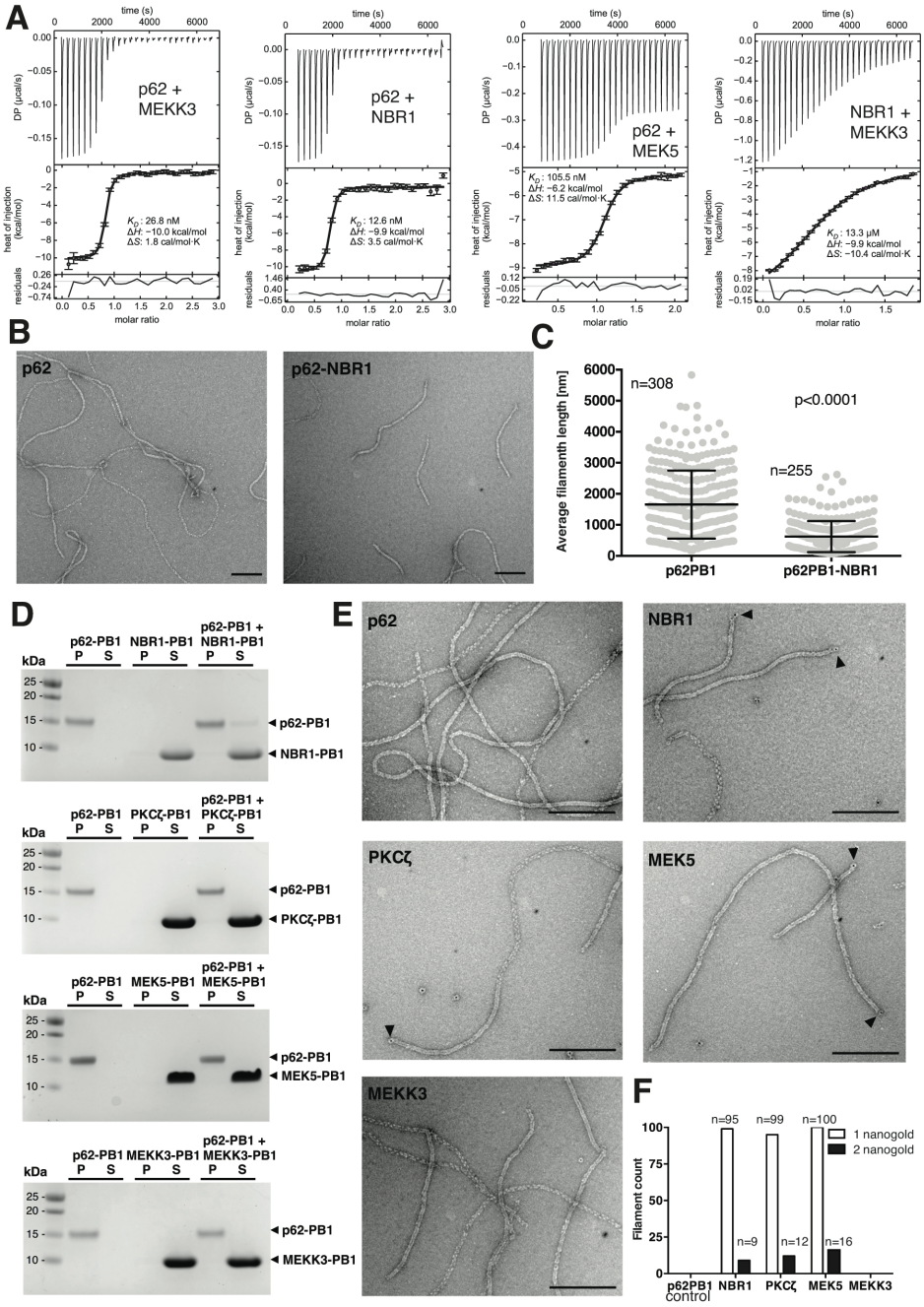

960

961 **Figure 4. Interactions of p62-PB1 with other PB1 domain proteins.**

962 (A) Quantitative determination of PB1 binding affinities by isothermal titration
963 calorimetry. Data represent mean and standard deviations from three
964 independent experiments. (B) Representative electron micrographs of
965 negatively stained p62-PB1$^{1-122}$ (left) and p62-PB1$^{1-122}$ incubated with human
966 NBR1-PB1 (right). (C) Quantification of filaments length of P62-PB1$^{1-122}$
967 filaments before and after incubation with NBR1-PB1. (D) Co-sedimentation

968 assays of p62-PB1$^{1-122}$ with NBR1-PB1, PKCζ-PB1, MEK5-PB1 and MEKK3-
969 PB1 (S = Supernatant; P = Pellet). Control experiments of p62-PB1$^{1-122}$ and the
970 respective PB1 interactor alone are also shown. (E) Representative electron
971 micrographs of negatively stained p62-PB1$^{1-122}$ with nanogold-labeled NBR1-
972 PB1, PKCζ-PB1, MEK5-PB1 or MEKK3-PB1. (F) Quantification of p62-PB1$^{1-122}$
973 filaments displaying one or two nanogold-labeled PB1 interaction domains.
974

975

Figure 5

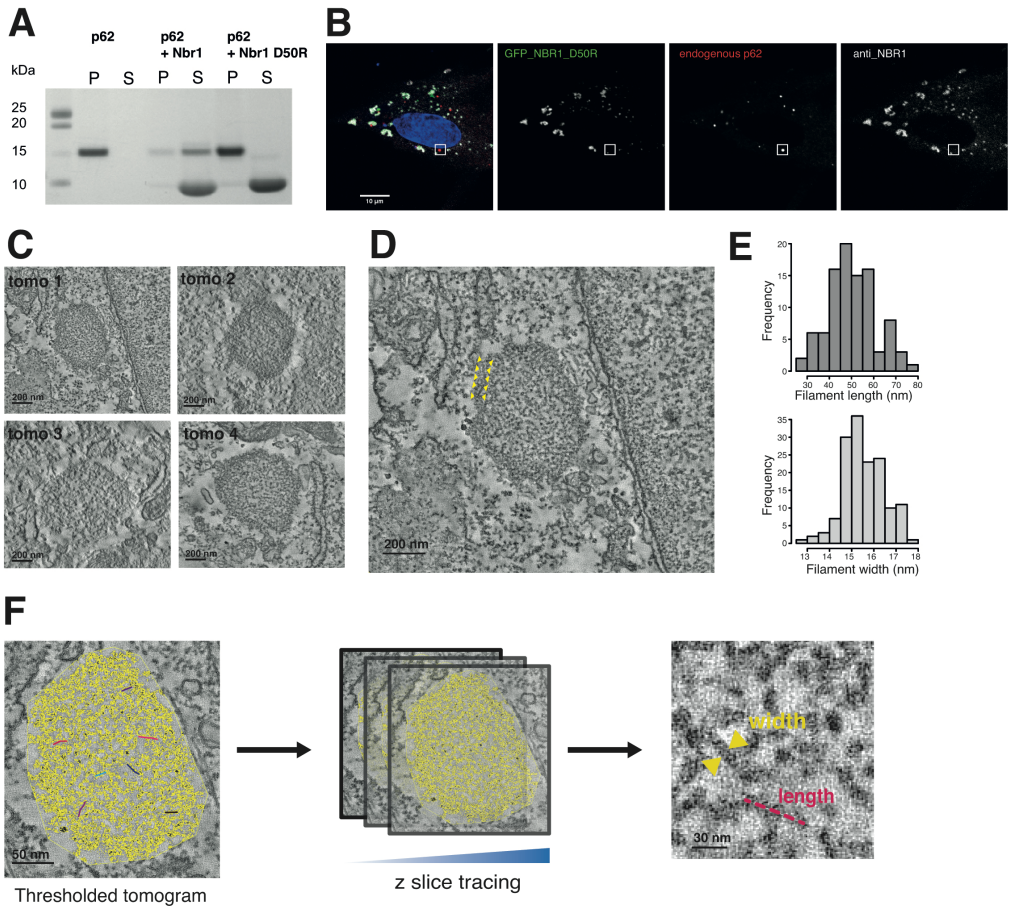

976

977 **Figure 5. CLEM visualization of p62 bodies in cells.**

978 (A) Effect of human NBR1-D50R mutation on p62 filaments. SDS-PAGE
979 analysis of pelletation assay showing that p62-PB1 filaments are not disrupted
980 by NBR1-PB1 with a D50R mutation (P = pellet; S = supernatant). (B)
981 Representative confocal fluorescence images showing p62 and NBR1 in RPE1
982 cells. Co-localization analysis of fixed RPE1 cells stably expressing
983 NBR1(D50R) shows no overlap of NBR1(D50R) with p62 bodies. (C)
984 Representative electron tomogram slices of p62 bodies localized by CLEM. (D)
985 Enlarged view of a representative tomogram slice from the highlighted p62
986 body in (B) reveals the filament-like meshwork of p62 bodies. Note the apparent
987 phase separation of the p62 body from the cytosol. The ring of increased
988 density surrounding the bodies is indicated by arrows. (E) Distribution of
989 estimated filament length and width from tracing in thresholded tomograms. (F)

990 Schematic illustration of width and length measurements performed in
991 thresholded tomograms.

Figure 6

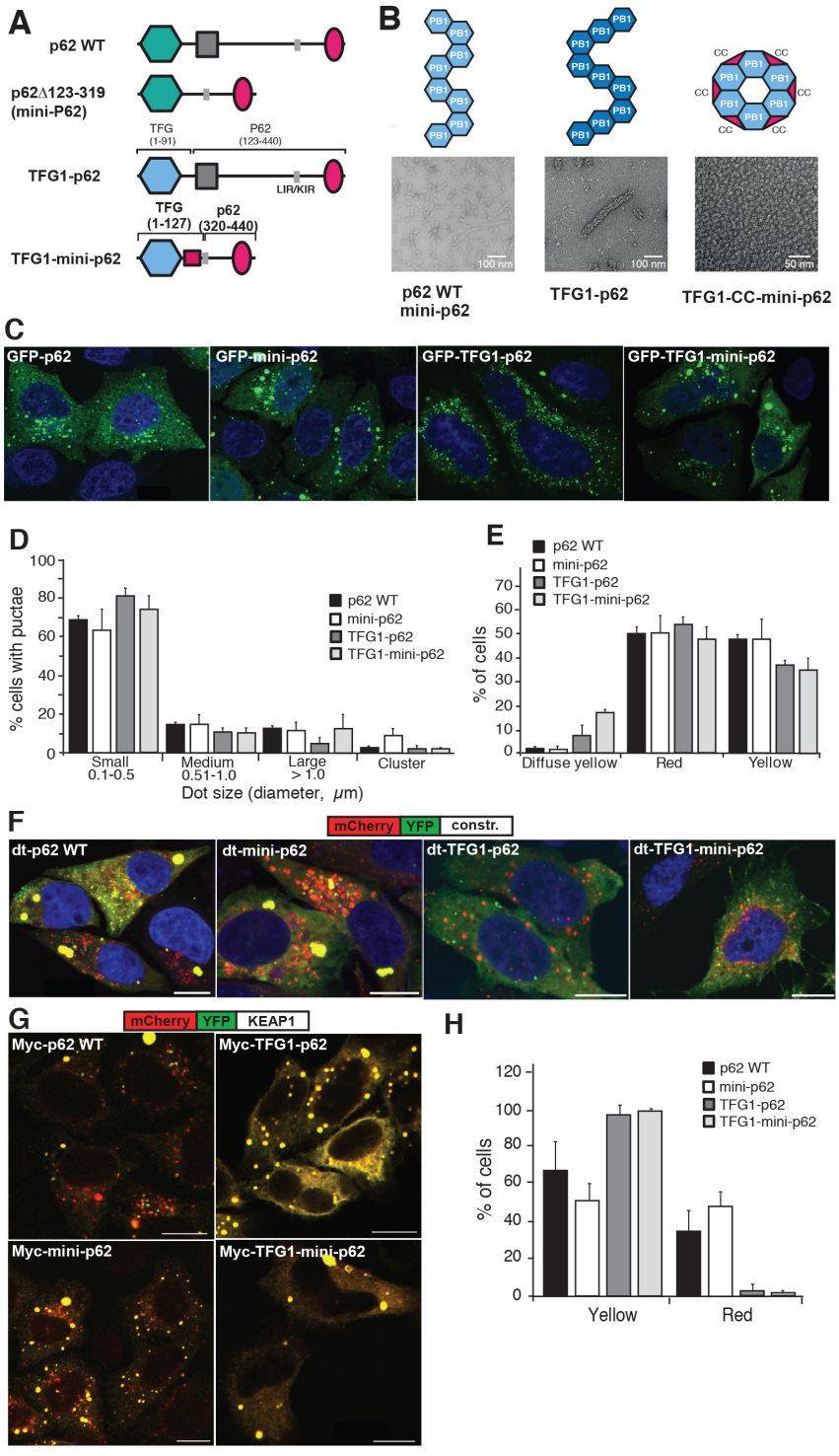

992

993 **Figure 6. Cellular assays of p62 polymeric state.**

994 (A) Schematic illustration of used p62 constructs and chimeras. (B)
995 Representative, negatively stained electron micrographs of purified p62

constructs and chimeras from (A) including illustration of polymeric and oligomeric forms observed by negative staining electron microscopy. (C) Confocal fluorescent images of HeLa p62 (KO) cells expressing GFP-tagged constructs and chimeras. All examined constructs form punctate structures. (D) Quantification of the number of p62 bodies forming dots of various size. (E) Quantification of cells displaying yellow and red dots in (F). (F) Representative confocal fluorescence images of HeLa p62 (KO) cells expressing mCherry-YFP-tagged (dt-tagged) p62 constructs and chimeras. The appearance of red puncta (as an indicator of lysosomal localization) for all constructs indicates that all constructs and chimeras can be processed by autophagy. Punctae were counted and classified based on more than 100 cells in each condition in three independent experiments. (G) Representative confocal fluorescence images of HeLa p62 (KO) cells expressing the respective p62 constructs and chimeras, as well as mCherry-YFP-tagged KEAP1. (H) Statistics of appearance of lysosome-localized and cytosolic dots for mCherry-YFP-tagged KEAP1.

1012

Figure S1

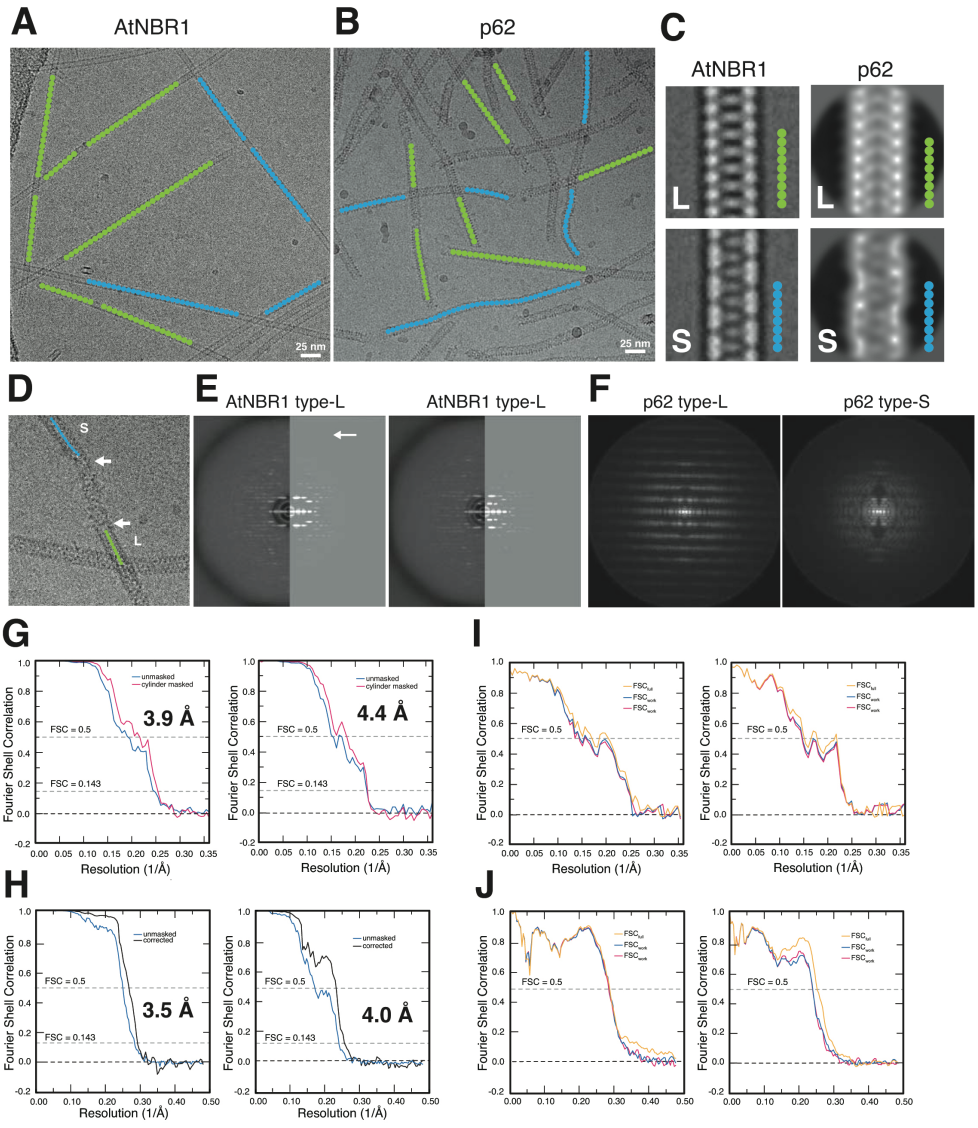

1013

1014 **Figure S1. Electron cryo-microscopy of AtNBR1-PB1 and p62-PB1.**

1015 (A) Representative micrographs of AtNBR1-PB1 with helix traces of segment
1016 centers classified as L-type (green) or S-type (blue) superposed. (B)
1017 Representative micrographs of p62-PB1 with center traces of segments
1018 classified as L-type (green) or S-type (blue) superposed. (C) Low-pass filtered
1019 class averages of L-type (top) and S-type (bottom) AtNBR1-PB1 and p62-PB1
1020 assemblies. (D) Representative image showing transitions between L and S-
1021 type assemblies for p62-PB1 (E) Side-by-side power spectra of L-type (top) and
1022 S-type (bottom) AtNBR1-PB1 assemblies with the power of sum of segments
1023 (left) and that simulated from re-projection of the 3D structure (right). Arrows

1024 indicate high-resolution meridional layer lines. (F) Power spectra of L-type (top)
1025 and S-type (bottom) p62-PB1 assemblies with the summed power spectra of
1026 the 2D classes. (G) Fourier shell correlation for 3D reconstruction of L-type (left)
1027 and S-type (right) AtNBR1-PB1 assemblies. (H) Fourier shell correlation for 3D
1028 reconstruction of L-type (left) and S-type (right) p62-PB1 assemblies. (I) Model
1029 vs. map Fourier shell correlation for L-type (left) and S-type (right) AtNBR1-PB1
1030 assemblies. (J) Model vs. map Fourier shell correlation for L-type (left) and S-
1031 type (right) p62-PB1 assemblies.

Figure S2

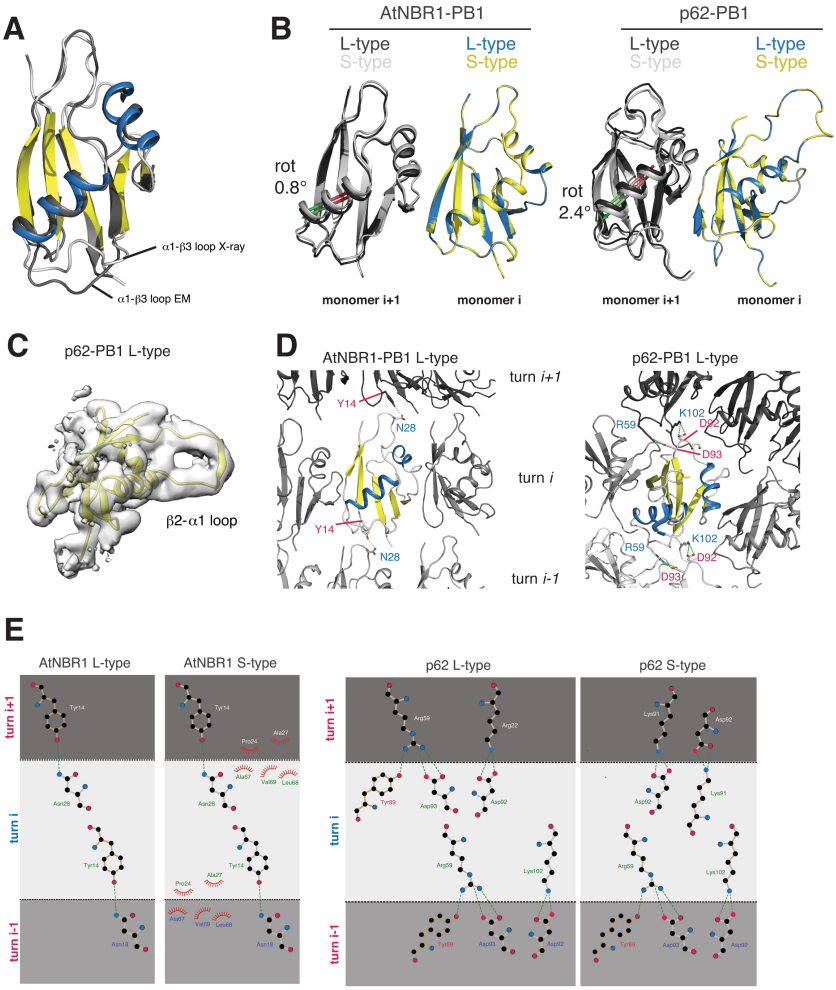

1032

1033 **Figure S2. Atomic models from crystal and cryo-EM structures of**
1034 **AtNBR1-PB1$^{1-95}$ and p62-PB1$^{1-122}$.**
1035 (A) Superposition of cartoon representation of atomic models from the 1.6 Å
1036 crystal structure of AtNBR1-PB1 and the de novo-built model based on the 3.9
1037 Å cryo-EM AtNBR1-PB1 density map. Marked differences are observed in loop
1038 regions mediating lateral contacts. (B) Superposition of atomic models for L-

type and S-type assemblies for AtNBR1-PB1 (left) and p62-PB1 (right). Monomer *i* for each assembly is superposed and the difference in rotation of adjacent subunit *i+1* are indicated. Only minor differences are observed. (C) LocScale map for L-type p62-PB1 cropped around one monomer. (D) Lateral contacts formed along the helical axis shown for AtNBR1-PB1 (left) and p62-PB1 (right). Subunits are shown in cartoon representation and relevant residue contacts are highlighted with side-chains shown as stick. (E) Schematic representation of common longitudinal contacts formed in AtNBR1-PB1 and p62-PB1 helices.

Figure S3

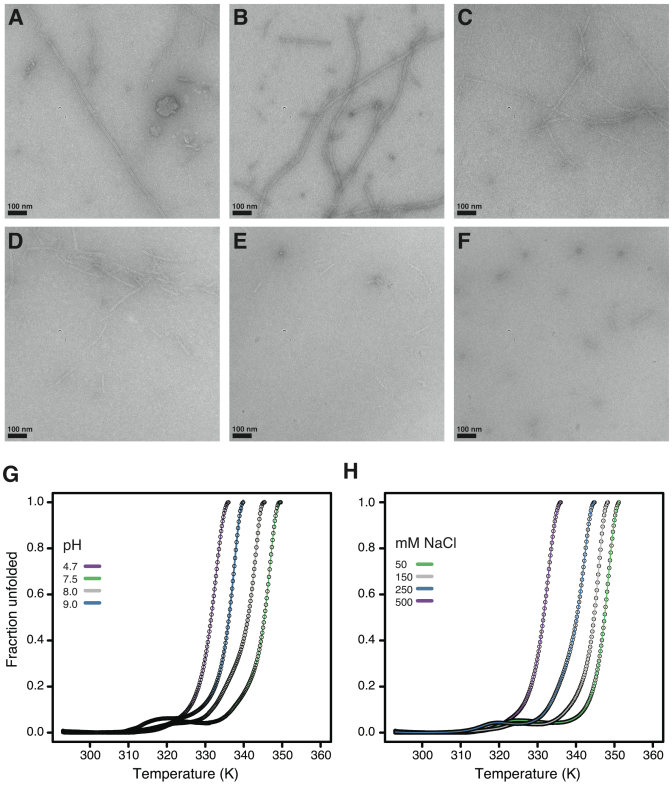

Figure S3. Electrostatic interactions drive type PB1 filament formation. (A-F) Negative-stain electron micrographs of AtNBR1-PB1 at increasing NaCl concentrations (A, 0 mM; B, 50 mM; C, 100 mM; D, 150 mM; E, 250 mM; F, 500 mM) illustrate how ionic strength weakens PB1 homo-oligomerization and affects filament length. (G/H) Thermofluor protein unfolding curves demonstrate that high ionic strength, as well as low and high pH destabilize a thermodynamically favorable (filamentous) state of AtNBR1-PB1.

Figure S4

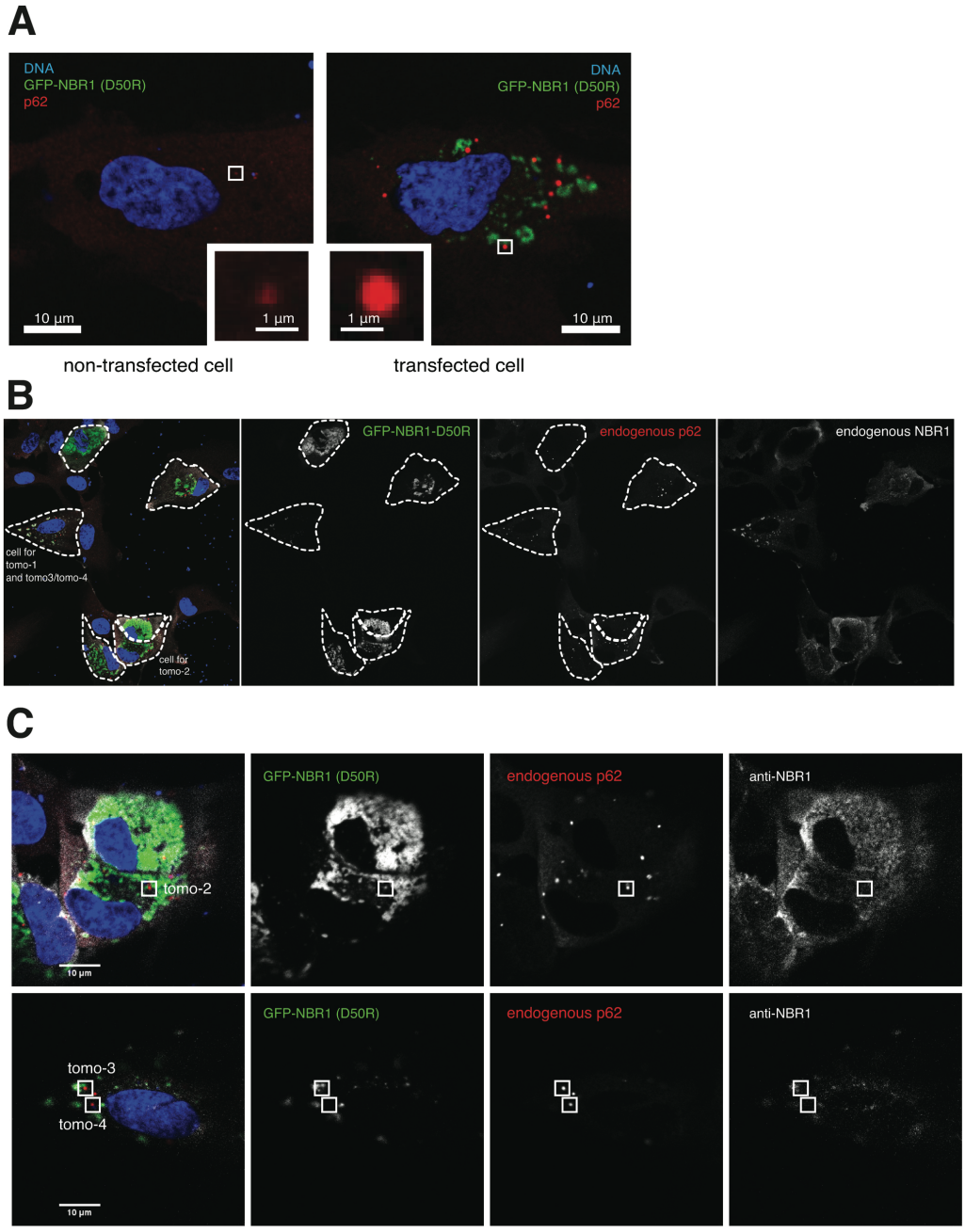

Figure S4. Fluorescence images of RPE1 cells.

(A) Representative confocal fluorescence image of RPE1 cells expressing or not expressing NBR1(D50R). Note the difference in average dot size of mCherry-p62 observed for both cases. (B) Overview fluorescence image showing the cells used for tomogram acquisition. Cells are outlined and the tomogram number is indicated. (C) Close-up view of cells in (B) indicating the subcellular position for tomogram acquisition.

Figure S5

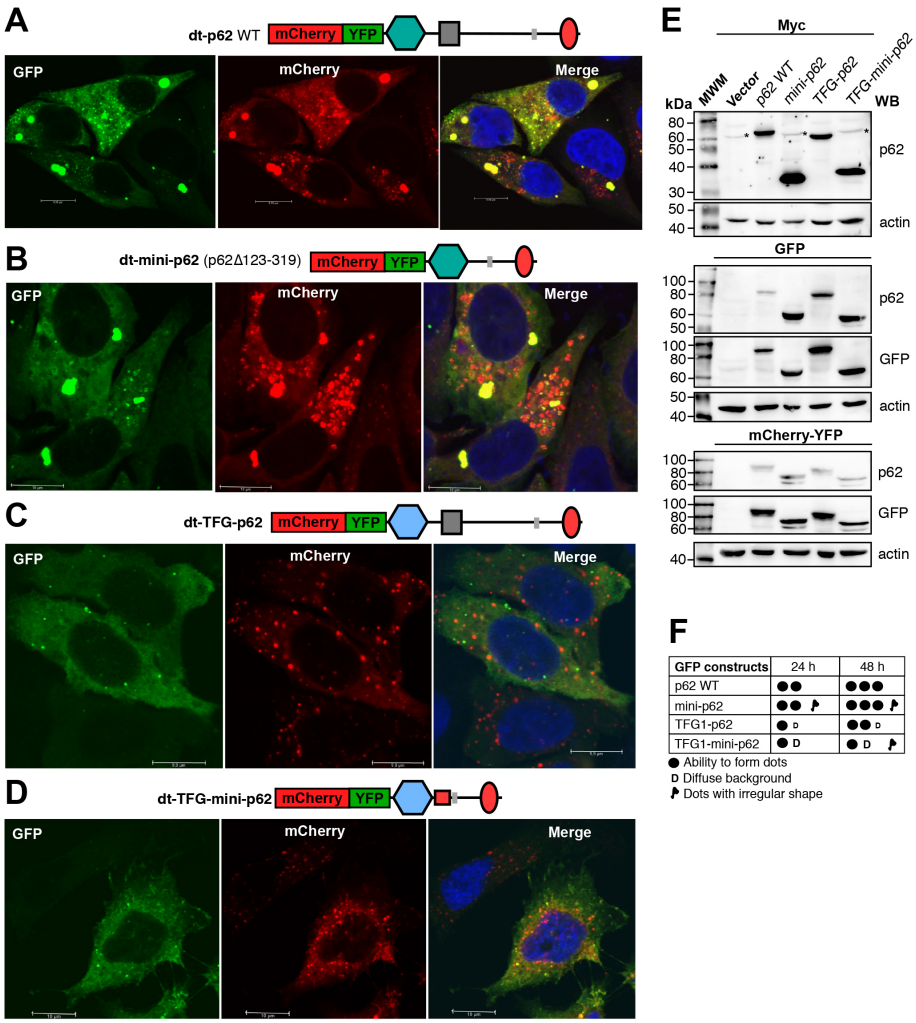

Figure S5. Chimera variants of p62 with the PB1 domain exchanged with a related domain from TFG is efficiently degraded by autophagy.

(A-D) Representative confocal images of HeLa p62 KO cells transiently transfected with the indicated p62 constructs fused to the mCherry-YFP double tag. Efficient degradation by autophagy is indicated by the accumulation of red-only dots. (E) Representative western blots using extracts from HeLa cells transiently transfected with the indicated p62 constructs fused to Myc (top), GFP (middle) or mCherry-YFP (bottom). p62, GFP or actin antibodies were used as indicated. (F) Graphic presentation of phenotypes observed by confocal imaging of cells transfected with p62 constructs fused to GFP (number of dots, morphology of dots, and amount of diffuse protein). Cells were analyzed 24h and 48h after transfection.

Figure S6

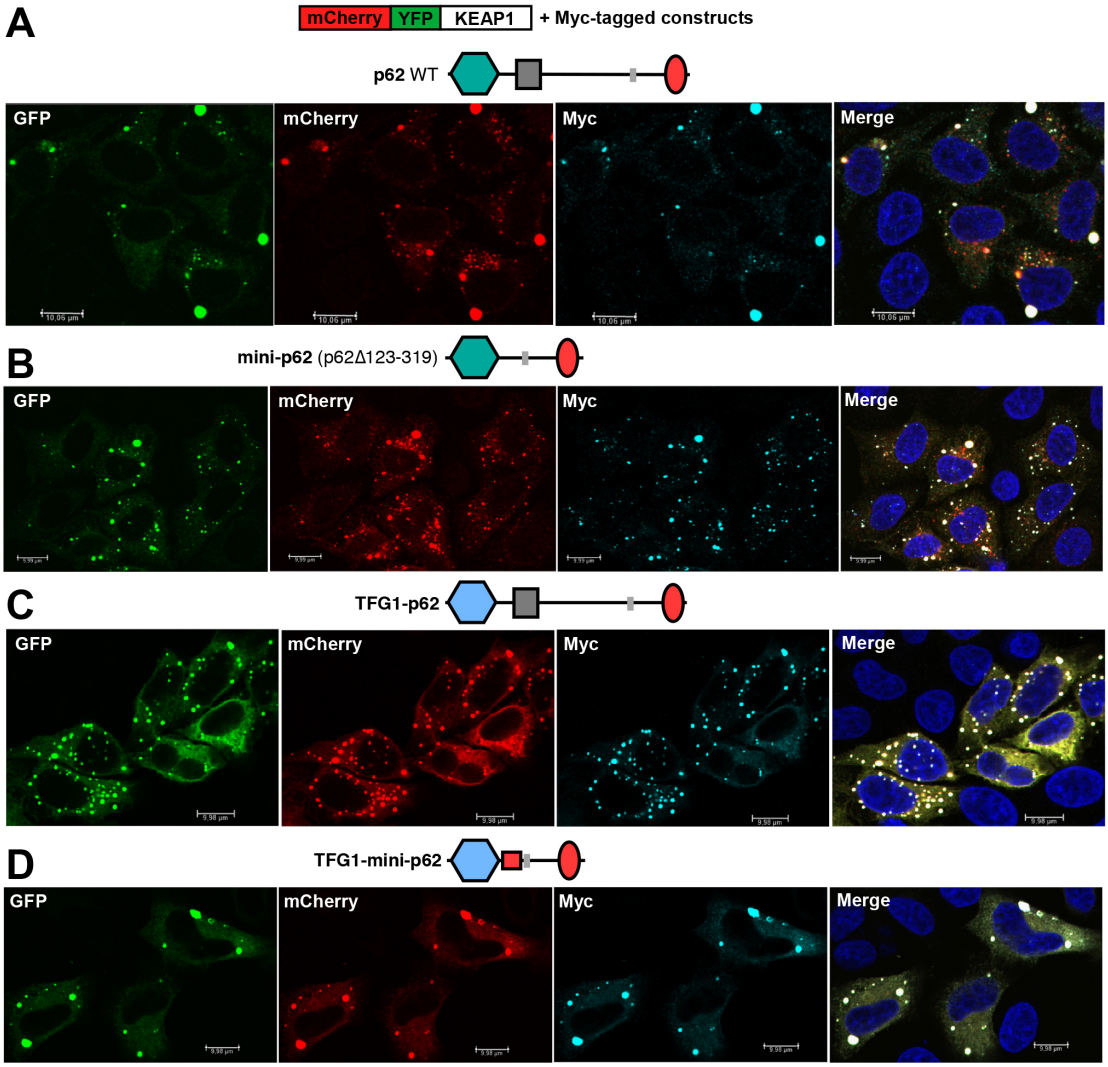

Figure S6. p62-mediated degradation of co-expressed KEAP1 depends on the native PB1 domain of p62.

(A-D) Representative confocal images of HeLa p62 KO cells transiently co-transfected with mCherry-YFP tagged KEAP1 and the indicated p62 constructs fused to Myc. Degradation of KEAP1 by autophagy (accumulation of red-only dots) is seen in cells co-transfected with full-length p62 or a mini-p62 deleted for residues 123-319, but not in cells co-transfected with chimera constructs containing the PB1 domain of TFG1.

Table S1. X-ray crystallography data collection and refinement statistics.

Data collection statistics	
Wavelength	
Resolution range	37.9 – 1.53 (1.585 - 1.53)
Space group	P 21 21 2
Unit cell	43.13 79.44 24.14 90 90 90
Total reflections	25830 (2499)
Unique reflections	13035 (1271)
Multiplicity	2.0 (2.0)
Completeness (%)	99.22 (99.30)
Mean I/sigma(I)	10.45 (1.42)
Wilson B-factor	20.99
R-merge	0.02799 (0.4132)
R-meas	0.03958 (0.5844)
R-pim	0.02799 (0.4132)
CC1/2	0.999 (0.655)
CC*	1.00 (0.89)
Model refinement	
Reflections used in refinement	13030 (1271)
Reflections used for R-free	669 (53)
R-work	0.2199 (0.3688)
R-free	0.2492 (0.4036)
CC(work)	0.943 (0.724)
CC(free)	0.937 (0.592)
Model refinement	
Number of non-hydrogen atoms	822
macromolecules	723
ligands	64
solvent	35
Protein residues	88
RMS (bonds)	0.007
RMS (angles)	0.79
Ramachandran	
favored (%)	100.00
allowed (%)	0.00
outliers (%)	0.00
Rotamer outliers (%)	2.60
Clashscore	3.47
Average B-factor	33.46
macromolecules	31.66
ligands	48.45
solvent	43.43

*Statistics for the highest-resolution shell are shown in parentheses.

Table S2. Cryo-EM data collection and model refinement statistics.

	AtNBR1-PB1$^{1-95}$ (EMD-XXXX, EMD-YYYY)	**p62-PB1$^{1-122}$** (EMD-XXXX, EMD-YYYY)
Data collection and processing		
Magnification	105kx	130kx
Voltage (kV)	300	300
Electron exposure (e$^-$/Å)	17	40
Defocus range (um)	1.0-4.0	0.5-2.5
Pixel size (Å)	1.386	1.040
Symmetry imposed	S-type: C1	S-type: C1
	L-type: C2	L-type: C2
Final no. particle images	S-type: 18,021	S-type: 51,679
	L-type: 25,387	L-type: 51,853
Helical rise (Å)	S-type: 5.905	S-type: 9.78
	L-type: 6.721	L-type: 4.787 (9.574)*
Helical twist (˚)	S-type: -31.17	S-type: -26.48
	L-type: -31.44	L-type: 77.29 (-25.42)*
Global map resolution (Å, FSC=0.143)	S-type: 4.4	S-type: 4.0
	L-type: 3.9	L-type: 3.5
Local map resolution range (Å)	S-type: 4.0 – 4.7	S-type: 3.7 – 4.4
	L-type: 3.4 – 4.1	L-type: 3.3 – 4.4

* equivalent notation for asymmetric unit of two monomers as described in the main text

	AtNBR1-PB1$^{1-95}$ (PDBXXX, PDBYYY)	**p62-PB1$^{1-122}$** (PDBXXX, PDBYYY)
Model refinement		
Initial model used (PDB code)	PDB-XYZ (X-ray model)	PDB ID 2kkc#
Model resolution (Å, FSC=0.5	S-type: 5.5	S-type: 4.0
	L-type: 4.3	L-type: 3.6
Map sharpening B-factor (Å^2)	S-type: -300	S-type: -193
	L-type: -200	L-type: -139
Model composition		
Non-hydrogen atoms	669 (S-/L-type)	808 (S-/L-type)
Protein residues	88 (S-/L-type)	104 (S-/L-type)
R.m.s. deviations		
Bond lengths (Å)	0.009/0.008 (S-/L-type)	0.006/0.007 (S-/L-type)
Bond angles (˚)	1.16/1.161 (S-/L-type)	1.22/1.24 (S-/L-type)
Validation		
MolProbity score	2.41/2.29 (S-/L-type)	1.94/1.64 (S-/L-type)
Clashscore*	7.59/6.41 (S-/L-type)	4.89/1.88/ (S-/L-type)
Rotamer outliers (%)	1.41/1.41 (S-L-type)	0.00/0.63 (S-/L-type)
Ramachandran plot		
Favored (%)	93.21/94.19 (S-/L-type)	83.33/83.33 (S-/L-type)
Allowed (%)	6.79/5.81 (S-/L-type)	16.67/16.67 (S-/L-type)
Disallowed (%)	0.00 (S-/L-type)	0.00 (S-/L-type)

* computed for 9-mer

[#] Saio, T., Yokochi, M., and Inagaki, F. (2009). The NMR structure of the p62 PB1 domain, a key protein in autophagy and NF-kappaB signaling pathway. J Biomol NMR *45*, 335–341.